

RICE UNIVERSITY

**Lifetimes of Weakly Bound Heavy-Rydberg
Ion-Pair States Formed through Rydberg Atom
Collisions with Attaching Targets**

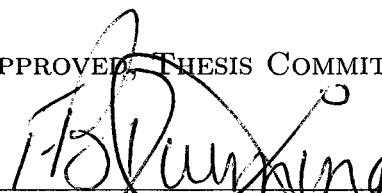
by

Changhao Wang

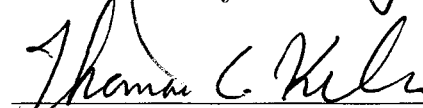
A THESIS SUBMITTED
IN PARTIAL FULFILLMENT OF THE
REQUIREMENTS FOR THE DEGREE

Master of Science


APPROVED, THESIS COMMITTEE:



F. B. Dunning, Chair
Sam and Helen Worden
Professor of Physics and Astronomy



T. C. Killian
Associate Professor of Physics and
Astronomy



M. D. Corcoran
Professor of Physics and Astronomy

Houston, Texas

April, 2010

UMI Number: 1486046

All rights reserved

INFORMATION TO ALL USERS

The quality of this reproduction is dependent upon the quality of the copy submitted.

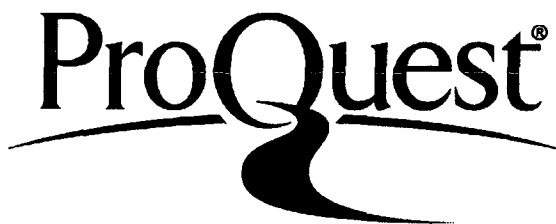
In the unlikely event that the author did not send a complete manuscript and there are missing pages, these will be noted. Also, if material had to be removed, a note will indicate the deletion.



UMI 1486046

Copyright 2010 by ProQuest LLC.

All rights reserved. This edition of the work is protected against unauthorized copying under Title 17, United States Code.



ProQuest LLC
789 East Eisenhower Parkway
P.O. Box 1346
Ann Arbor, MI 48106-1346

Lifetimes of Weakly Bound Heavy-Rydberg Ion-Pair States Formed through Rydberg Atom Collisions with Attaching Targets

Changhao Wang

Abstract

The formation of $K^+ \cdots Cl^-$ heavy-Rydberg ion-pair states through dissociative electron attachment in $K(np)/CCl_4$ collisions is investigated. The product ion-pair states are detected directly by electric field-induced dissociation. A Monte Carlo collision code is used to analyze the results that models both the initial Rydberg electron attachment and the subsequent evolution of the ion pairs. The data and the calculations demonstrate the production of long-lived bound $K^+ \cdots Cl^-$ heavy-Rydberg ion pairs. They also suggest that collinear collisions can generate heavy-Rydberg states of low angular momentum.

Acknowledgments

I would not have finished this thesis without the help of several people. Many thanks first go to Dr. Barry Dunning, my advisor, for his insightful ideas and patient guidance, which makes the lab work conducted progressively. I would also like to thank my senior student, Matt Cannon, who shared his detailed points of running the whole apparatus. I also benefits from other colleagues in the lab, Jeff Mestayer, Dennis Neufeld, Brendan Wyker, Yu Pu, Shuzhen Ye, for their contributions to this work.

In particular, my greatest thanks are given to my parents, whose support and encouragement from my childhood continually pushed me to who I am right now.

Contents

| | |
|--|----------|
| Abstract | ii |
| Acknowledgments | iii |
| List of Figures | vi |
| 1 Introduction | 1 |
| 1.1 Rydberg Atoms | 2 |
| 1.2 Heavy Rydberg Systems | 3 |
| 2 Creation of Heavy Rydberg Systems | 6 |
| 2.1 Production of Rydberg Atoms | 7 |
| 2.1.1 Quantum defect | 7 |
| 2.2 Crossed Beams and Velocity Selection | 9 |
| 2.3 Electron Attachment to Molecules | 10 |
| 2.3.1 Non-dissociative Electron Attachment | 11 |
| 2.3.2 Dissociative Electron Attachment | 13 |
| 2.4 Field Ionization and Dissociation | 15 |
| 2.5 Monte Carlo Simulation | 17 |

| | | |
|----------|---|-----------|
| 3 | Experimental Apparatus and Techniques | 20 |
| 3.1 | Vacuum System | 21 |
| 3.2 | Laser System | 22 |
| 3.3 | Potassium Beam | 23 |
| 3.4 | Interaction Region | 25 |
| 3.5 | Time-of-Flight Mass Spectrometry | 27 |
| 4 | Results and Analysis | 29 |
| 4.1 | Electric Field-Induced Dissociation | 29 |
| 4.2 | Lifetime Measurements | 37 |
| 4.3 | Orbital Properties | 44 |
| 4.3.1 | Collinear Beams | 47 |
| 5 | Conclusions and Future Work | 52 |
| 5.1 | Conclusions | 52 |
| 5.2 | Future Work | 52 |
| | Bibliography | 54 |
| A | Calculations of the Potassium Beam Density | 56 |

Figures

| | | |
|-----|--|----|
| 2.1 | n dependence of the quantum defect for potassium atoms. | 9 |
| 2.2 | Energy diagrams for nuclear-excited Feshbach resonances | 12 |
| 2.3 | Energy diagrams for dissociative electron attachment | 14 |
| 2.4 | Electron potential energy in a uniform static electric field | 16 |
| | | |
| 3.1 | Schematic diagram of the experimental apparatus. | 21 |
| 3.2 | Velocity distribution of potassium atoms and beams | 25 |
| 3.3 | Time sequence of the laser pulse and field pulses within the interaction region | 26 |
| 3.4 | Presence of the magnetic field deflects electrons | 28 |
| | | |
| 4.1 | Energy distribution of $K^+ \cdots Cl^-$ ion pairs | 30 |
| 4.2 | Time-of-flight spectra of Cl^- ions observed in $K(20p)/CCl_4$ collisions | 31 |
| 4.3 | The Rydberg atom velocity dependence of the escape fraction observed in $K(20p)/CCl_4$ collisions | 32 |

| | | |
|------|---|----|
| 4.4 | Distribution of n_H and ℓ_H of $K^+ \cdots Cl^-$ ion pairs for Rydberg atom velocities indicated | 33 |
| 4.5 | K^+ signals observed as a function of applied field | 35 |
| 4.6 | Cl^- signals observed as a function of applied fields | 36 |
| 4.7 | Time-of-flight spectra of Cl^- signals observed following $K(16p)/CCl_4$ collisions with a small extraction field | 38 |
| 4.8 | Time development of the population of bound $K^+ \cdots Cl^-$ heavy-Rydberg ion-pair states | 39 |
| 4.9 | Time-of-flight spectra of Cl^- ion signals observed in $K(20p)/CCl_4$ collisions with the delay variation of the second pulsed fields indicated | 41 |
| 4.10 | Time development of the population of bound $K^+ \cdots Cl^-$ heavy-Rydberg ion-pair states dissociated by the second pulsed field | 43 |
| 4.11 | Distribution of n_H and ℓ_H of $K^+ \cdots Cl^-$ ion pairs for the values of n indicated | 45 |
| 4.12 | Calculated angular momentum distribution of heavy-Rydberg ion-pair states formed in $K(16p)/CCl_4$ collisions for the Rydberg atom velocities indicated | 46 |
| 4.13 | Calculated periapsis distribution of heavy-Rydberg ion-pair states formed in $K(16p)/CCl_4$ collisions with the Rydberg atom velocities indicated | 47 |
| 4.14 | Velocity distributions of potassium atomic and SF_6 molecular beams | 48 |

| | | |
|------|--|----|
| 4.15 | Relative velocity distributions for a background target gas and collinear beams | 50 |
| 4.16 | Angular momentum distributions for a background target gas and collinear beams | 51 |
| A.1 | Sketch of the hot wire detector | 57 |

Chapter 1

Introduction

Rydberg states are produced when one electron in an alkali atom is excited to a state of very large principal quantum number n . Because of their large physical size and weak binding energy, their properties are quite unlike those normally associated with atoms in ground or low-lying excited states. At sufficiently high n (> 50), the distance between the excited electron and the core ion is so large that in collisions with neutral molecules they behave independently, allowing studies of collision processes dominated by the electron-target interaction, including electron attachment to polyatomic molecules. Rydberg atom collisions with attaching targets at high n mostly result in creation of an (unbound) positive core ion and a negative ion. However, at intermediate n ($\sim 16 - 50$), collisions can lead to formation of bound ion-pair states termed heavy-Rydberg or heavy-electron states, comprising a positive and negative ion pair orbiting at large separations weakly bound by their mutual Coulomb attraction. In many respect, heavy Rydberg states are analogous to atomic Rydberg states, but their extremely large reduced mass and much higher principal quantum number lead to some significant differences. Heavy Rydberg states lie at the boundary of quantum and classical behavior and provide an interesting system to explore the crossover between the two regimes. In some cases, these systems can be treated

as a classical macroscopic system.

1.1 Rydberg Atoms

An atom in a Rydberg state has a valence electron in a large orbit far from the core ion. The electron feels an almost hydrogenic Coulomb potential and the binding energy is given by:

$$E_B = -\frac{R_\infty}{n^2} \quad (1.1)$$

where $R_\infty = 109737.32 \text{ cm}^{-1}$ is the Rydberg constant. However, the mass of the atomic nucleus is not actually infinite compared to that of the electron, leading to a reduced-mass correction to the Rydberg constant

$$R_M = \frac{R_\infty}{1 + m_e/M} \quad (1.2)$$

where m_e and M are the mass of the electron and the atomic nucleus respectively. On the other hand, the inner electrons do not entirely screen the nuclear charge. In particular, for low orbital angular momentum states of complex atoms, there is a significant probability of finding the excited electron near the nucleus where the wavefunctions of the inner electrons and the Rydberg electron overlap. The resulting shift in the binding energy is represented by the quantum defect δ_{nlj} and the corrected binding energy is given by:

$$E_B = -\frac{R_M}{(n - \delta_{nlj})^2} \quad (1.3)$$

Table 1.1 : n dependence of properties of Rydberg atoms

| Property | Scaling(a.u.) | $n = 1$ | $n = 20$ | $n = 40$ | $n = 60$ |
|----------------------|-------------------|------------------------|-----------------------|-----------------------|-----------------------|
| Mean Radius | n^2 | 0.05 nm | 20 nm | 85 nm | 190 nm |
| Orbital Period | n^3 | 0.15 fs | 1.2 ps | 9.8 ps | 33 ps |
| Velocity | $\frac{1}{n^3}$ | 2.2×10^6 m/s | 1.1×10^5 m/s | 5.5×10^4 m/s | 3.6×10^4 m/s |
| Binding Energy | $\frac{1}{n^2}$ | 13.6 eV | 34 meV | 8.5 meV | 3.8 meV |
| Energy Spacing | $\frac{1}{n^3}$ | 10.2 eV | 3.2 meV | 0.4 meV | 0.1 meV |
| Classical Field | $\frac{1}{16n^4}$ | 3.2×10^8 V/cm | 2008 V/cm | 125 V/cm | 25 V/cm |
| Ionization Threshold | | | | | |

Rydberg atoms in states of high principal quantum number n have unusual characteristics compared to atoms in the ground or low-lying states. This is illustrated in Table 1.1 which lists a variety of atomic properties with their dependence on n and numerical values at specific n . The mean atomic radius increases rapidly with n , whereas the binding energy and the classical field ionization threshold decrease rapidly. At $n = 60$ the binding energy is only 3.8 meV, and a field of 25 V/cm is sufficient to ionize the atom.

1.2 Heavy Rydberg Systems

A heavy Rydberg system is a molecular system that is weakly bound by the Coulomb potential between a positive/negative ion pair [1]. It can be viewed as an atom with the Rydberg electron replaced by a massive negative ion. Their dimensions and

binding energies are similar to those of Rydberg atoms, but the orbital periods are much longer.

The large increase in the reduced mass, given by

$$\mu = \frac{M_1 M_2}{M_1 + M_2}, \quad (1.4)$$

where M_1 and M_2 are the mass of two ions forming the ion-pair state, leads to a dramatic increase in the effective Rydberg constant for heavy-Rydberg states given by

$$R_{\text{H}} = \frac{\mu}{m_e} R_{\infty} \quad (1.5)$$

Typically the ratio μ/m_e varies from 10^4 to 10^6 . Table 1.2 lists the physical quantities important in discussing atomic Rydberg states, their values expressed in fundamental constants m_e , e , \hbar , ϵ_0 and c , along with equivalent quantities for heavy Rydberg states. Numerical values for the $\text{K}^+ \cdots \text{SF}_6^-$ ion-pair states are included.

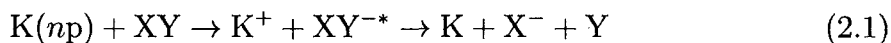
Table 1.2 : Atomic unit for electronic Rydberg systems and ion-pair units for heavy Rydberg systems. The last column is given for $K^+ \dots SF_6^-$ ion-pairs with the ratio $M = \mu/m_e = 56221.5276$.

| Quantity | Symbol | Expression | SI value | IP units | SI value($K^+ \dots SF_6^-$) |
|------------------|------------|---------------------------------------|-------------------------------------|-------------|--|
| Mass | m_e | m_e | 9.109×10^{-31} kg | Mm_e | 5.121×10^{-26} kg |
| Action | \hbar | \hbar | 1.054×10^{-34} Js | \hbar | 1.054×10^{-34} Js |
| Charge | e | e | 1.602×10^{-19} C | e | 1.602×10^{-19} C |
| Length | a_0 | $4\pi\epsilon_0\hbar^2/m_e e^2$ | 5.287×10^{-11} m | a_0/M | 9.404×10^{-16} m |
| Time | τ_0 | $(4\pi\epsilon_0)^2\hbar^3/m_e e^4$ | 2.416×10^{-17} s | τ_0/M | 4.297×10^{-22} s |
| Velocity | v | $e^2/4\pi\epsilon_0\hbar$ | 2.188×10^6 m/s | v | 2.188×10^6 m/s |
| Energy | E_0 | $m_e e^4/(4\pi\epsilon_0)^2\hbar^2$ | 4.363×10^{-18} J | ME_0 | 2.453×10^{-13} J |
| Potential | U_0 | $m_e e^3/(4\pi\epsilon_0)^2\hbar^2$ | 27.23 V | MU_0 | 1.531×10^6 V |
| Electric Field | F_0 | $m_e^2 e^5/(4\pi\epsilon_0)^3\hbar^4$ | 5.150×10^{11} V/m | M^2F_0 | 2.895×10^{16} V/m |
| Magnetic Field | B_0 | $m_e^2 e^3/(4\pi\epsilon_0)^2\hbar^3$ | 2.353×10^5 T | M^2B_0 | 1.323×10^{10} T |
| Rydberg Constant | R_∞ | $E_h/2hc$ | 1.098×10^7 m ⁻¹ | MR_∞ | 6.173×10^{11} m ⁻¹ |

Chapter 2

Creation of Heavy Rydberg Systems

Heavy-Rydberg ion-pair states have been generated in such simple molecules as H_2 and HF by multistep laser-induced photoexcitation. The dipole selection rules $\Delta J = 0, \pm 1$ only allow excitation of a limited range of low-angular-momentum (low J) states. Higher J states can be accessed by application of a DC field which leads to Stark precession and periodic changes in J , for studies of the dynamics of $\text{H}^+ \cdots \text{H}^-$ [1] and $\text{H}^+ \cdots \text{F}^-$ [2] ion-pair states. However, heavy-Rydberg ion-pair states are also created through electron transfer in collisions between Rydberg atoms and electron attaching targets via reactions of the type [3]



A Monte Carlo collision code is used to analyze such reactions that models both the initial Rydberg electron attachment and the subsequent evolution of the ion pairs. The product ion-pair states are detected using electric field-induced dissociation and a time-of-flight spectrometer.

2.1 Production of Rydberg Atoms

Rydberg atoms have been produced by charge exchange, electron impact excitation, and photoexcitation [4], through reactions of the type



Koch [5] provided a discription of using charge exchange to convert a fast ion beam to a fast beam of Rydberg atoms. Schiavone et al. [6] used electron impact to excite ground state atoms to Rydberg states and to redistribute the initially excited atoms to low ℓ states. Photoexcitation, which is used in our experiment, differs from the above two methods by allowing excitation of the specific final states. By specifying the energy (or wavelength) of the incident photons, targeted final (low- ℓ) states can be obtained.

2.1.1 Quantum defect

To account for core penetration of the excited electron and incomplete screening of the nuclear potential at small r , which leads to tighter binding of (penetrating) low- ℓ states, a quantity $\delta_{n\ell j}$, called the quantum defect, is introduced to give an effective principal quantum number $n^* = n - \delta_{n\ell j}$, the energy level being given by

$$E(n, \ell, j) = -\frac{hcR_M}{(n - \delta_{n\ell j})^2} \quad (2.6)$$

Table 2.1 : Potassium quantum defect parameters.

| Series | δ_0 | δ_2 | δ_4 | δ_6 | δ_8 |
|------------|--------------|------------|------------|------------|------------|
| $ns_{1/2}$ | 2.180197(15) | 0.136(3) | 0.0759 | 0.117 | -0.206 |
| $np_{1/2}$ | 1.713892(30) | 0.2332(50) | 0.16137 | 0.5345 | -0.234 |
| $np_{3/2}$ | 1.710848(30) | 0.2354(60) | 0.11551 | 1.105 | -2.0356 |

where n , ℓ and j specify the energy of an excited state. The quantum defect $\delta_{n\ell j}$ is slightly n dependent only when $n < 10$ (shown in Fig. 2.1), and is specified for individual j states. To be explicit, the quantum defect of a particular $n\ell j$ state can be obtained using the expression [4]

$$\delta_{n\ell j} = \delta_0 + \frac{\delta_2}{(n - \delta_0)^2} + \frac{\delta_4}{(n - \delta_0)^4} + \frac{\delta_6}{(n - \delta_0)^6} + \frac{\delta_8}{(n - \delta_0)^8} + \dots \quad (2.7)$$

where the values of the parameters δ_0 , δ_2 , \dots for potassium atoms are given in Table 2.1. To photoexcite a ground state potassium atom from the ground 4s state to a selected np state, the wavelength of the laser must be tuned such that

$$\frac{hc}{\lambda} = E_i - E(n, \ell, j) \quad (2.8)$$

where E_i is the ionization energy of potassium.

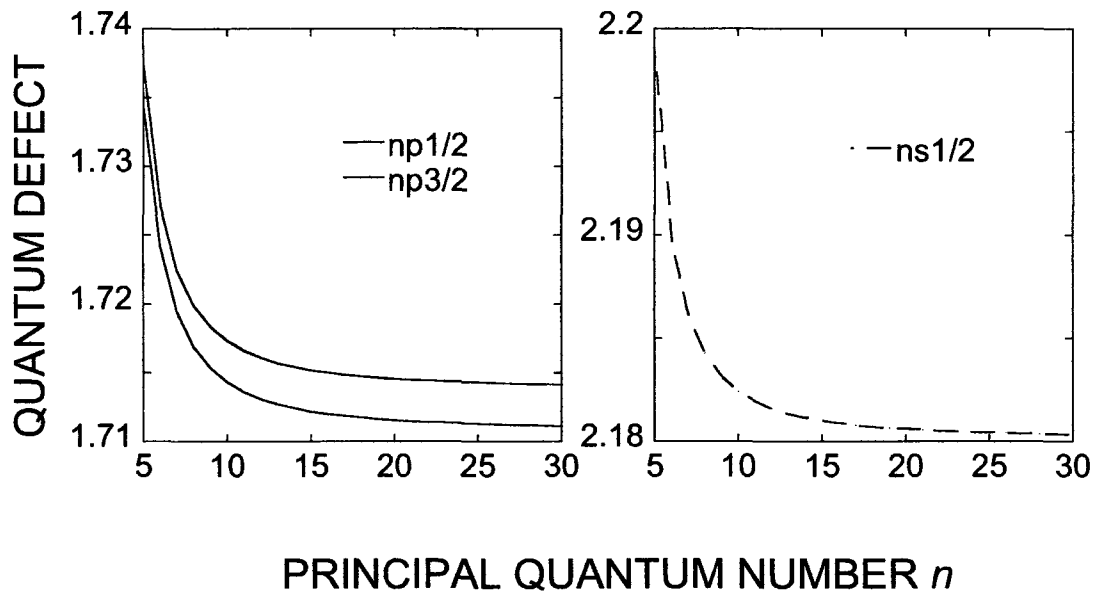


Figure 2.1 : n dependence of the quantum defect for potassium atoms.

2.2 Crossed Beams and Velocity Selection

In the present work potassium atoms contained in a collimated beam are excited using a crossed laser beam. The laser beam intersects the atomic beam at a small angle θ off of normal incidence, allowing the excitation of Rydberg atoms with only a narrow range of velocities. For an atom moving with the velocity $v \ll c$, the Doppler effect gives the relationship between the intrinsic transition frequency f_0 in the atomic frame and the laser frequency f in the lab frame [7]

$$f \simeq f_0 \left(1 + \frac{v}{c} \sin \theta\right)^{-1} \quad (2.9)$$

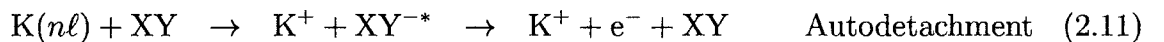
which, since $v \ll c$, can be further approximated as

$$f \simeq -\left(\frac{f_0}{c} \sin \theta\right)v + f_0 \quad (2.10)$$

where the velocity v of the excited atoms depends linearly on the laser frequency f . The Rydberg atom velocity is determined by observing their motion using a position-sensitive detector.

2.3 Electron Attachment to Molecules

At high n ($n \gtrsim 10$) the separation of the core ion and the excited electron becomes such that they do not interact simultaneously with a (neutral) target molecule, i.e., the atom behaves as a pair of independent scatters. In essence, the atom can be viewed as a low-energy electron trap. Collisions with molecules that attach low-energy electrons can thus lead to reaction of the type [8]:



where the excited anion XY^{-*} is the transient intermediate, which might undergo rapid autodetachment forming a neutral molecule and a free electron (reaction 2.11),

or (if the electron remains bound to the K^+ core ion) to creation of another $n'\ell'$ Rydberg state and a neutral molecule (reaction 2.12). In reaction 2.13, the intermediate is temporarily stabilized by internal vibrational energy relaxation leading to formation of a long-lived metastable negative ion. In reaction 2.14, electron capture results in fragmentation of the intermediate ion producing a neutral and a negative ion. Of interest here are the last two reactions, which are usually termed non-dissociative and dissociative electron transfer, respectively.

2.3.1 Non-dissociative Electron Attachment

Electron attachment to molecules proceeds via a negative-ion resonant state (NIRS) [8], a nonstationary time-dependent state with a characteristic autodetachment lifetime τ . For many polyatomic molecules, long lived ($\tau > 10^{-6}$) intermediates XY^{-*} can be formed via nuclear-excited Feshbach resonances, as illustrated in Fig. 2.2. Here the kinetic energy of the captured electron is used to excite molecular vibrations without electronic excitation of the target molecule. The negative-ion state lies energetically below the parent ground state, resulting from a positive electron affinity (EA). Here the electron affinity is defined as the difference in energy between the neutral molecule plus an electron at rest at infinity and the molecular negative ion when both neutral molecule and negative ion are in their ground electronic, vibrational and rotational states.

Following electron capture, the excess internal energy which includes the electron

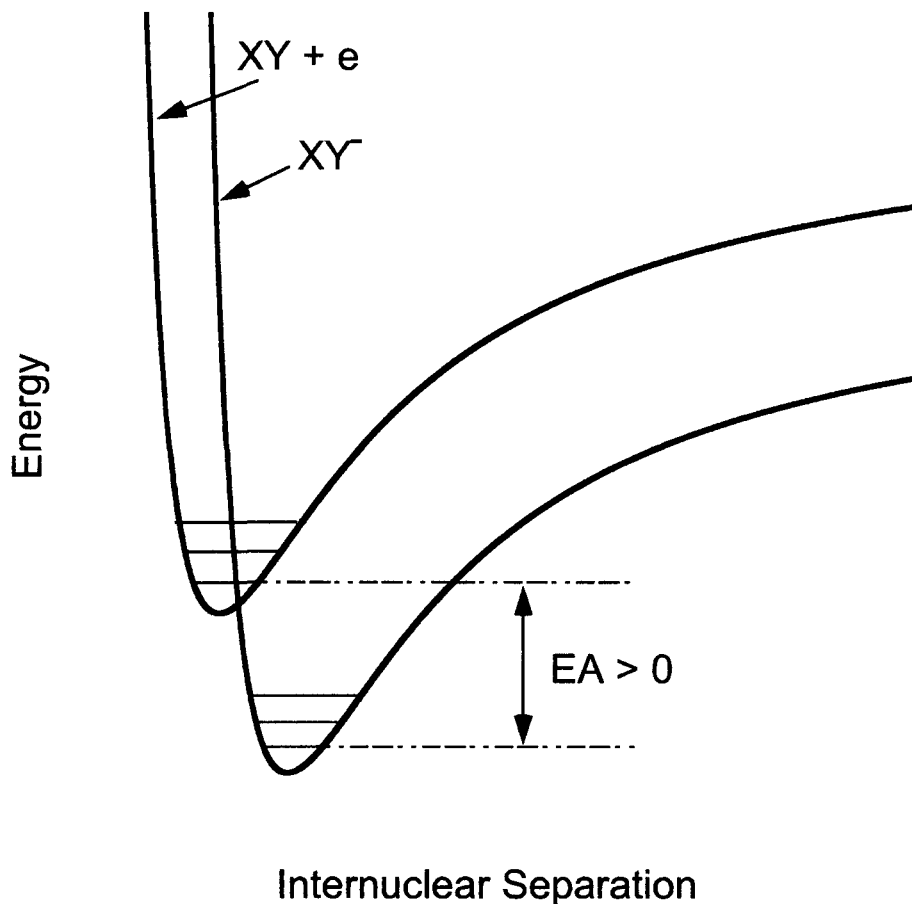


Figure 2.2 : Schematic energy diagrams for nuclear-excited Feshbach resonances with a positive EA.

affinity of the molecule, the kinetic energy of the captured electron and the initial molecular vibrational energy can be rapidly redistributed within the negative ion. This can happen if the excess energy of the reaction is localized in a few attaching vibrational modes of the molecules. Subsequently, these excited modes are in turn coupled to other vibrational modes. In this process, called intramolecular vibrational energy redistribution (IVR), the excess energy of reaction is widely distributed making it unlikely to be reconcentrated in a mode from which autodetachment can occur.

IVR therefore leads to the formation of long-lived metastable negative ions XY^- (reaction 2.13).

2.3.2 Dissociative Electron Attachment

Fragmentation of the intermediate ion following electron attachment in reaction 2.14 produces a neutral and a negative ion, a process termed dissociative electron attachment (DEA). Molecules undergoing such dissociation are treated as diatomic or diatomic-like molecules XY . DEA happens energetically only when fragment Y has a positive electron affinity, forming a stable negative ion Y^- . Halogen negative ions [9–11] (F^- , Cl^- , Br^- , I^-) are typically involved in DEA because of their large EA. DEA is a resonant process of two stages. Electrons are first captured by the target molecule in a vertical transition between potential energy curves from the equilibrium positions of the atoms according to the Franck-Condon principle. The resulting transient intermediate then dissociates into the final product X and Y^- .

The postattachment process following the initial capture is determined by the position and shape of the potential energy curve for XY^{-*} relative to that for the molecule XY . In Fig. 2.3a, the asymptote ($X + Y^-$) of the the XY^{-*} curve lies below that ($X + Y$) of the XY curve by an amount equal to the electron affinity $EA(Y)$ of Y . The potential energy curve for XY^{-*} gives a repulsive process at $R > R_c$, resulting in dissociative attachment. However, in the region of $R < R_c$, where the potential energy curve of XY^{-*} lies above that of XY , the molecular negative ion is unstable

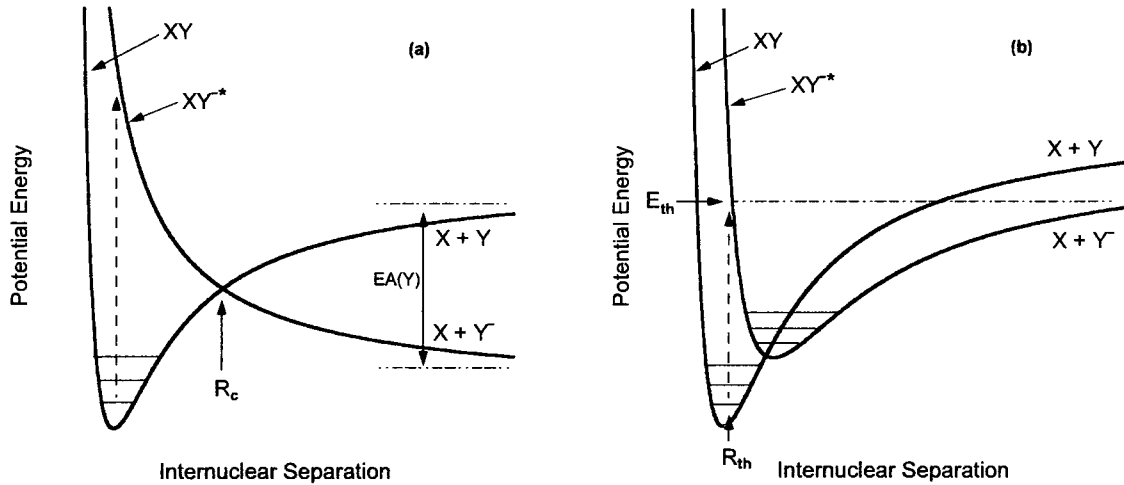


Figure 2.3 : Schematic potential energy diagrams for dissociative electron attachment to diatomic molecules.

toward electron ejection, leading to autoionization as well as to fragmentation.

As far as dissociative attachment is concerned, another postattachment case, where both dissociative and nondissociative electron attachment can occur, is shown in Fig. 2.3b. In the potential energy curve for XY^{-*} , an attractive potential energy well is formed. The products at the threshold E_{th} are formed with essentially zero kinetic energy. Therefore, dissociation of the intermediate formed is energetically possible for a limited range of the internuclear separation $R < R_{th}$. Transitions induced by electron capture in the distance range of $R > R_{th}$ will temporarily produce vibrationally excited negative ions XY^{-*} , a fraction of which may subsequently dissociate.

2.4 Field Ionization and Dissociation

The weak binding energy makes Rydberg atoms sensitive to applied electric fields. In a uniform static electric field F applied in the $+z$ direction, the potential experienced by the excited electron is given by

$$V = -\frac{1}{r} + Fz \quad (2.15)$$

A saddle point appears on the $+z$ axis, as shown in Fig. 2.4, located at $z_s = -1/\sqrt{F}$, with potential energy $V_s = -2\sqrt{F}$. In a state with magnetic quantum number $m = 0$, where there is no additional centrifugal potential. If the electron is bound by an energy E , a field

$$F = \frac{E^2}{4} \quad (2.16)$$

is then needed to ionize the atoms classically, i.e., to allow simple over-the-barrier escape. This is usually called the classical field ionization threshold. If the Stark shift in the energy of Rydberg states is ignored, the binding energy is simply

$$E = -\frac{1}{2n^2} \quad (2.17)$$

where the classical field ionization is given in terms of the principal quantum number n by (Table 1.1)

$$F = \frac{1}{16n^4} \quad (2.18)$$

Actually, the centrifugal barrier $1/(x^2 + y^2)$ for $m \neq 0$ states keeps the electron

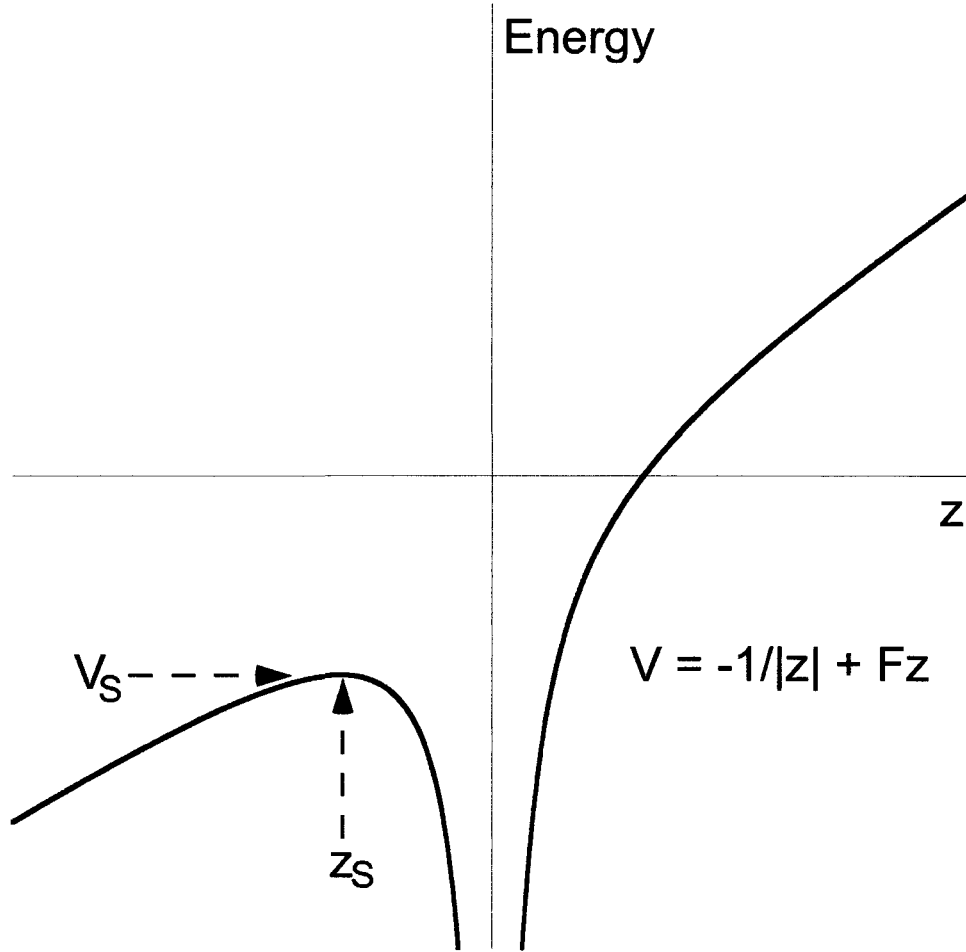


Figure 2.4 : Potential energy for an electron in a uniform static electric field applied in the z direction.

away from the z axis, raising the threshold field compared to an $m = 0$ state by

$$\frac{\Delta F}{F} = \frac{|m|\sqrt{E}}{\sqrt{2}} = \frac{|m|}{2n} \quad (2.19)$$

For the extreme red Stark state, the corrected binding energy is given using the linear Stark effect by

$$E = -\frac{1}{2n^2} - \frac{3n^2 F}{2} \quad (2.20)$$

Using this energy we find the corrected threshold field

$$F = \frac{1}{9n^4} \quad (2.21)$$

If the binding energy E_B of heavy-Rydberg ion pairs is above the saddle point in Fig. 2.4, ionization, termed field dissociation, then occurs through a classical over-the-barrier escape. The field required to ionize the ion pairs scales as $F \propto E_B^2$.

2.5 Monte Carlo Simulation

The formation of bound ion-pair states in collisions between atoms in high Rydberg states and target molecules is studied using a semiclassical Monte Carlo code that models the detailed kinematics of electron transfer reactions [12]. It is based on an independent particle picture and attachment is viewed as a binary interaction between the Rydberg electron and the target molecule. The probability density distribution of the excited electron is determined by its principal quantum number n . The initial velocities of the Rydberg atoms follow a Maxwell speed distribution, as discussed in detail in Section 3.3. Considering the Doppler broadening of the laser frequency, the velocities of Rydberg atoms are chosen from a Gaussian distribution averaged on v_0 with the standard deviation σ_v

$$P_{Rydberg}(v) = \frac{1}{\sqrt{2\pi}\sigma_v} e^{-\frac{(v-v_0)^2}{2\sigma_v^2}} \quad (2.22)$$

Given that the target molecule velocity distribution (which also follows a Maxwell speed distribution) is isotropic, each velocity component of a target molecules is

chosen at random from a Gaussian distribution

$$P_{target}(v) = \frac{1}{\sqrt{\pi}\alpha} e^{-\frac{v^2}{\alpha^2}} \quad (2.23)$$

where $\alpha = \sqrt{\frac{2kT}{m}}$ is the most probable velocity and m is the molecule mass. The probability of electron capture at some point is taken to be proportional to the local electron probability density and independent of collision velocity. To compensate for the quantum defect ($\delta_{nlj} \simeq 1.71$) of potassium atoms, the experiment for a particular $K(np)$ state is modelled using a $(n - 2)p$ hydrogenic state.

Following electron capture, in the case of the dissociative electron attachment, the intermediate is presumed to dissociate after some time interval t governed by

$$P(t) = \frac{e^{-\frac{t}{\tau}}}{\tau} \quad (2.24)$$

where τ is the mean lifetime of the intermediate (typically a few picoseconds or less). The angular distribution of the fragments is considered to be isotropic in the rest frame of the intermediate. Efficient redistribution of the excess energy of reaction within the intermediate prior to dissociation [13] results in a two-dimensional Boltzmann translational energy release distribution of the form

$$P(\epsilon) = \frac{e^{-\epsilon/\bar{\epsilon}}}{\bar{\epsilon}} \quad (2.25)$$

where $\bar{\epsilon}$ is the mean translational energy release.

The total energy of the product ion pair is calculated by

$$E_{tot} = E_k + E_p + E_{vib} \quad (2.26)$$

$$= \frac{1}{2}\mu v^2 - \frac{e^2}{4\pi\epsilon_0 r} + E_{vib} \quad (2.27)$$

where E_{vib} is an empirical term added to take into account the molecular vibrational energy transfer into translational energy of the ion pair. If $E_{tot} > 0$, the ion pair is able to overcome their mutual electrostatic attraction and separate. If $E_{tot} < 0$, bound ion-pair states are formed. The orbital properties of each ion pair such as the periapsis, eccentricity and angular momentum are then calculated.

Chapter 3

Experimental Apparatus and Techniques

The present apparatus is shown schematically in Fig. 3.1. Potassium atoms contained in a thermal-energy collimated beam are photoexcited to selected np states using the crossed output of a frequency-doubled Rhodamine 6G dye laser. The laser beam is incident a small angle ($\sim 2.5^\circ$) off normal to the potassium beam to selectively excite atoms with a relatively narrow velocity distribution (~ 100 m/s FWHM) by tuning the laser to the appropriate point in the Doppler profile. Experiments are conducted in a pulsed mode, the laser output being chopped into a train of pulses using an acousto-optic modulator. The interaction region is defined by two parallel photomesh grids of 100 lines per inch, separated by ~ 3.3 mm. Excitation occurs in the presence of background target gas. Following the laser pulse, voltage pulses are applied to either the lower grid or the upper grid after a predetermined time, producing a pulsed field F across the interaction region. Depending on the field polarization either positive or negative ions are accelerated into the drift region associated with a time-of-flight (ToF) mass spectrometer. Upon exiting the drift region they are detected by a position sensitive detector (PSD) [14] that records their arrival times and positions.

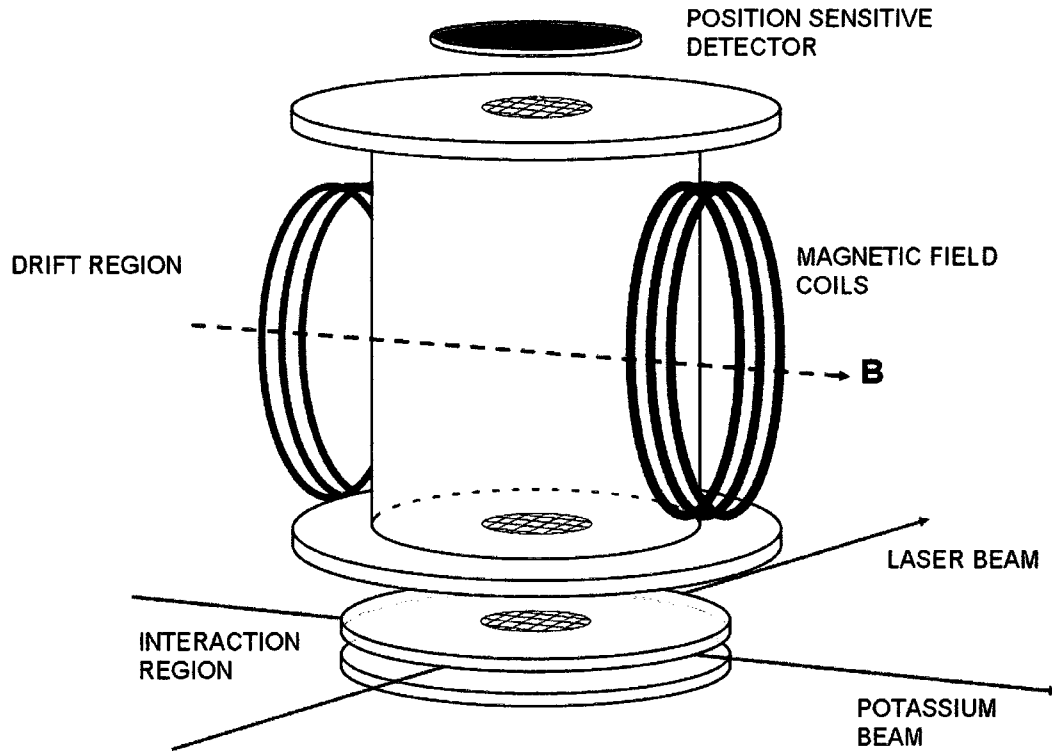


Figure 3.1 : Schematic diagram of the experimental apparatus.

3.1 Vacuum System

The vacuum system consists of two pumped regions: the oven chamber and the main chamber, separated by a 0.3 mm diameter aperture. The oven chamber contains an oven in which potassium metal is heated to 300°C to produce an effusive beam, which enters the main chamber through a small aperture. The main chamber contains the interaction region in which the Rydberg atoms are created, the drift region for the ToF Mass Spectrometry, and the PSD. The chambers are pumped by a combination

of mechanical and diffusion pumps, and their pressure (typically $\sim 2.0 \times 10^{-7}$ torr without the target gases and $\sim 1.0 \times 10^{-5}$ in the presence of gases) is monitored using a hot cathode Bayard-Alpert ion gauge. The laser beam enters and exits the main chamber through quartz windows set at Brewster's angle.

3.2 Laser System

The ionization energy of the potassium 4s electron is 4.34 eV, which corresponds to a wavelength of 286 nm. The wavelengths required to photoexcite ground state atoms to the selected np states ($n \sim 16-50$) in the experiments is in the range of 286-290 nm. This radiation is generated using a Coherent Verdi V8 laser, a CR-699-21 Rh6G dye laser and a Spectra-Physics Wavetrain frequency doubler.

The Verdi V8 is a diode-pumped solid-state laser which supplies a stable 532 nm, 7.5 W pump beam. This is focused into a jet of Rh6G dye in ethylene glycol in the dye laser. Rhodamine 6G has a single frequency tuning range of $\sim 565-600$ nm. A three-plate birefringent filter with a passive bandwidth of 380 GHz, a thick (10 mm) etalon with a free-spectral-range (FSR) of 10 GHz, and a thin (0.5 mm) etalon with a 200 GHz FSR combine to achieve single frequency operation, giving an effective output line width of ≤ 500 kHz.

The long-term drift (~ 40 GHz/hr) in the output frequency of the CR-699-21 is actively controlled by locking it to a frequency stabilized Helium-Neon (HeNe) laser using a confocal Fabry-Perot etalon (the superlock system). The orthogonally polar-

ized dye and HeNe beams are passed collinearly through the etalon which is scanned using a piezoelectric transducer (PZT), and then are separated using a polarizing beam splitter. As the PZT drive voltage changes, two transmission peaks are selected, one corresponding to each of the superposed beams. Any deviation of the dye laser frequency will shift its associated transmission peak relative to the HeNe laser peak. The changes in relative peak spacing are used to generate an error signal to compensate for the dye laser drift. This superlock system therefore maintains the long-term frequency stability of the dye laser output to <1 MHz/day.

The frequency-stabilized output of the dye laser is directed into the Wavetrain frequency doubler. A beta-Barium-Borate (BBO) crystal is used inside the resonator block to produce a harmonic output beam by nonlinear second harmonic generation. An acousto-optic modulator (AOM) is used to chop the output beam into pulses with duration of ~ 150 ns - 2 μ s every 50 μ s. The first order diffracted beam from the AOM is directed into the main chamber via a Brewster window while beams of other orders are blocked.

3.3 Potassium Beam

In the oven chamber, potassium metal is heated up to 300 °C, well above the melting point (63.38 °C) and below the boiling point (759 °C). The potassium vapor density n_0 is mainly determined by the temperature T of the oven body. A straightforward order-of-magnitude estimate of the vapor density can be obtained by assuming the

dynamic equilibrium between the liquid potassium and its vapor

$$n_0 \sim \aleph \exp\left(-\frac{\mathcal{W}}{k_B T}\right) \quad (3.1)$$

where \aleph is the liquid density, and \mathcal{W} is the work required to pull an atom out of the liquid. For potassium, $\aleph \sim 1.3 \times 10^{22} \text{ cm}^{-3}$, and $\mathcal{W} \sim 0.8 \text{ eV}$. Therefore, $n_0 \sim 1.0 \times 10^{15} \text{ cm}^{-3}$ at $T = 300 \text{ }^\circ\text{C}$, corresponding to a vapor pressure of $\sim 0.06 \text{ Torr}$. The mean free path of the vapor is $\sim 1 \text{ mm}$, larger than the size (0.5 mm) of the collimation aperture which is kept at a higher temperature (320 $^\circ\text{C}$) to prevent potassium from condensing and blocking it. The atom flow through this aperture is essentially effusive and further collimated by a 0.3 mm aperture located between the oven chamber and the main chamber. The combination of two apertures results in a beam divergence of $\sim 0.6^\circ$. The beam density decreases rapidly as the potassium atoms move away from the oven, and is measured by a hot wire detector in the main chamber, and estimated to be $\sim 10^9 \text{ cm}^{-3}$ near the center of the interaction region.

The velocity distribution of potassium in an effusive beam is given by [15]

$$P_{beam}(v) = \frac{1}{2} \left(\frac{m}{k_B T}\right)^2 v^3 e^{-\frac{mv^2}{2k_B T}} \quad (3.2)$$

where it is different from that in the oven (a Maxwell speed distribution), both given in Fig. 3.2 at $T = 300 \text{ }^\circ\text{C}$, because the faster atoms have larger probabilities of escaping through the apertures and entering the main chamber. As a result, the average velocity in the beam \bar{v}_b is larger than that in the oven \bar{v}

$$\bar{v}_b = \frac{3}{4} \sqrt{\frac{2\pi k_B T}{m}} \quad (3.3)$$

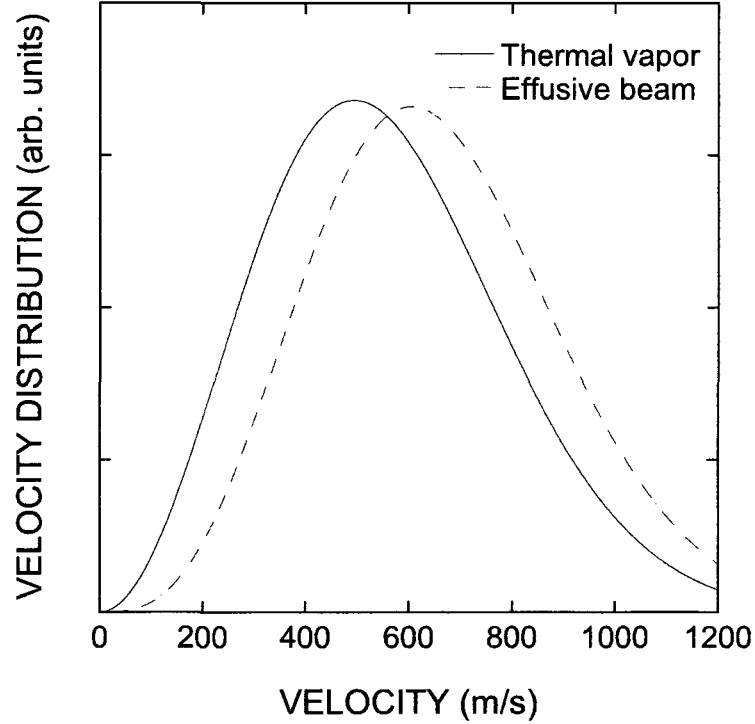


Figure 3.2 : Velocity distribution of potassium for the thermal vapor and the effusive beam at $T = 300^\circ\text{C}$.

or

$$\bar{v}_b = \frac{3\pi}{8}\bar{v} \quad (3.4)$$

For potassium, $\bar{v}_b = 658 \text{ m/s}$ at $T = 300^\circ\text{C}$.

3.4 Interaction Region

Excitation of potassium atoms and their collisions with target molecules occur near the center of an interaction region defined by two parallel photomesh grids separated by $\sim 3.3 \text{ mm}$. Either positive or negative voltages can be applied to both upper

and lower grids to ionize the heavy-Rydberg ion pairs and extract ions out of the interaction region to be detected.

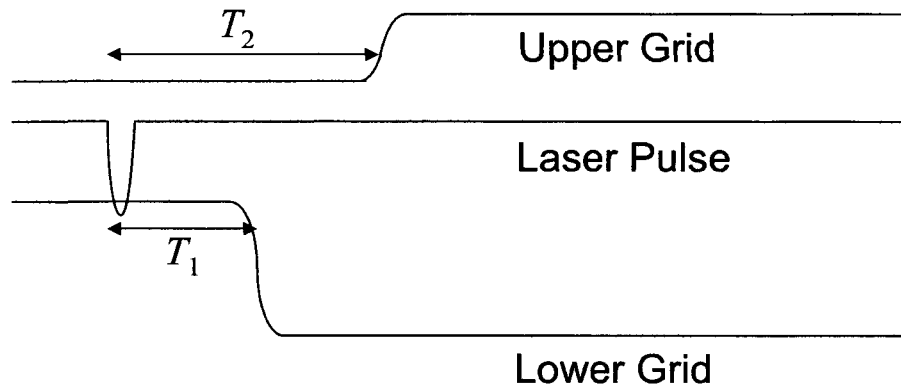


Figure 3.3 : Time sequence of the laser pulse and field pulses within the interaction region.

The experiment is conducted in a pulse mode with data being accumulated over many pulses. A typical cycle is illustrated in Fig. 3.3. A laser pulse with duration of at least ~ 150 ns excites potassium atoms to the selected np states. After a given time interval T_1 when Rydberg atoms collide with target molecules, a large pulsed field with a risetime of $\sim 1\mu\text{s}$ is applied to the lower grid while the upper grid is kept grounded. The amplitude of this electric field is typically sufficient to field ionize remaining parent np Rydberg atoms and to dissociate the more weakly bound ion-pair states. After another given time interval T_2 relative to the laser pulse, a second pulsed field is, if needed, applied to the upper grid which creates larger electric fields across the interaction region to dissociate even more tightly bound-ion pairs. The time evolution of those bound ion pairs with specific binding energies can

be investigated by varying the time delay T_1 and T_2 . In this way, either positive or negative ions extracted from the interaction region can be detected by the PSD.

3.5 Time-of-Flight Mass Spectrometry

Reactions are analyzed with the aid of a time-of-flight mass spectrometer comprising, as illustrated in Fig. 3.1, a drift region ~ 12.5 cm long and ~ 6.3 cm in diameter. Ion flight times are varied by changing the potential on the meshes that define the drift region. Charged particles are finally detected upon exit from the drift region by a position sensitive detector (PSD) with a circular active area of ~ 25 mm in diameter. The PSD has two microchannel plates and a resistive anode which gives the position distribution. The arrival time distribution is used to determine the decay (or build-up) of the population of a specific ion, whereas the position distribution gives information on the initial positions of the ions and their flight paths.

To discriminate against electrons generated by blackbody-radiation-induced photoionization and field ionization of parent Rydberg atoms a transverse magnetic field is established across the drift region using a pair of magnetic coils. The effects of the field are illustrated in Fig. 3.4 using SF_6 target molecules. In the absence of a magnetic field, the arrival position distributions for both SF_6^- ions produced in $\text{K}(20\text{p})/\text{SF}_6$ collisions and electrons produced by blackbody-radiation-induced photoionization are similar and centered within the detection region. As the magnetic field is increased the SF_6^- arrival position distribution remains essentially unchanged.

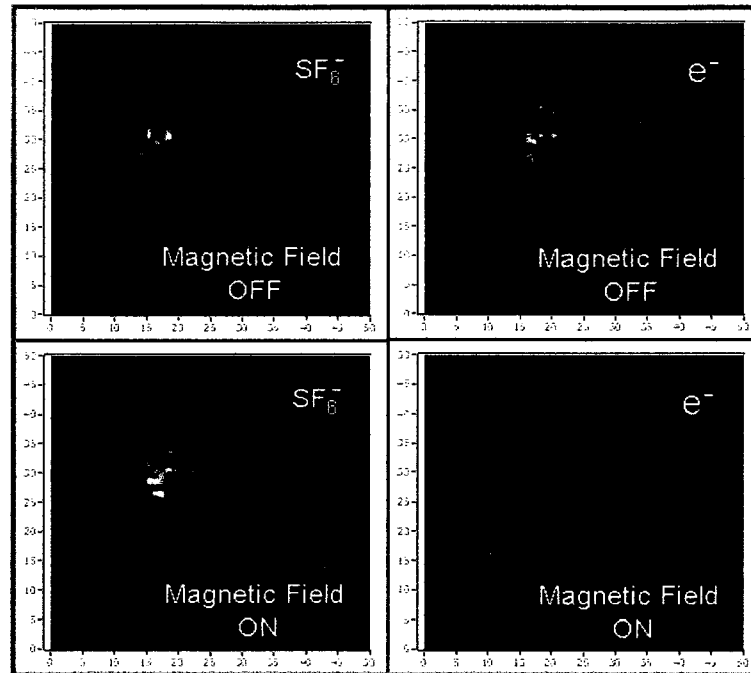


Figure 3.4 : Presence of the magnetic field deflects electrons.

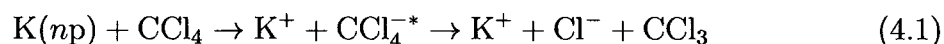
The electrons, however, are deflected until, at fields of a few gauss none can reach the PSD. Instead, they strike the tube of the drift region and are lost. Secondary electrons are discriminated against by biasing the exit aperture from the drift region negative with respect to the drift tube.

Chapter 4

Results and Analysis

4.1 Electric Field-Induced Dissociation

In the present work heavy-Rydberg $K^+ \cdots Cl^-$ ion-pair states are formed through dissociative electron transfer in collisions between Rydberg atoms and the attaching target CCl_4 via reactions of the type



where the lifetime τ of the intermediate CCl_4^{-*} is ~ 7.5 ps, and the mean translational energy release $\bar{\epsilon}$ is ~ 0.1 eV, the majority of which is acquired by the lighter Cl^- fragment.

The calculated distribution of the final energies of product $K^+ \cdots Cl^-$ ion pairs formed in collisions between $K(16p, 20p, 30p$ and $50p)$ atoms and CCl_4 molecules for Rydberg atom velocities of 200 m s^{-1} and 900 m s^{-1} is shown in Fig. 4.1. The energy distribution is wide and results mainly from the broad translational energy release distribution that accompanies dissociation of the CCl_4^{-*} intermediate. The binding becomes stronger as n is decreased because the size of the electron cloud is reduced and attachment occurs closer to the K^+ core ion. However, even at $n = 30$ a significant fraction of the ion pairs is bound, especially at the lower Rydberg velocity,

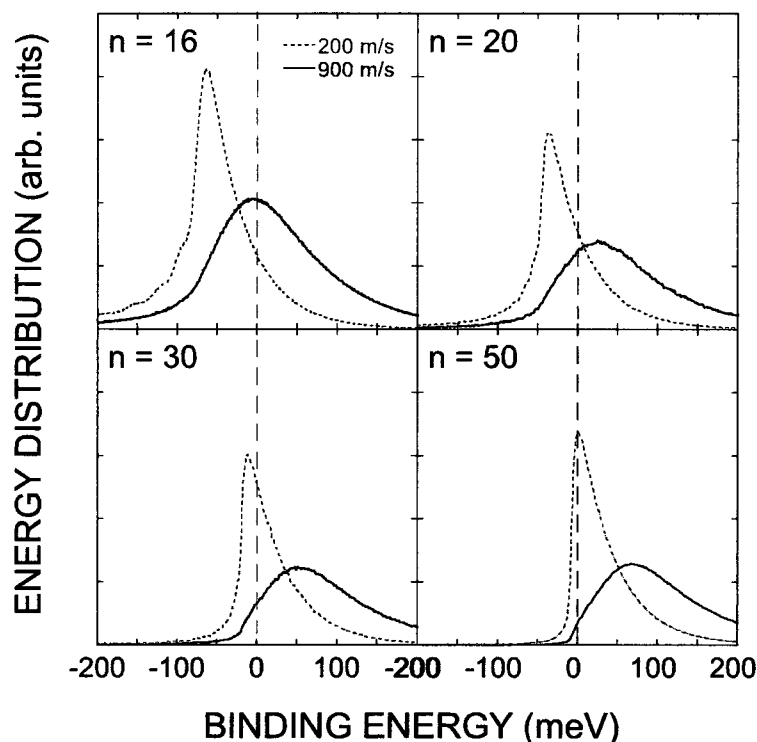


Figure 4.1 : Calculated final energy distribution of $K^+ \cdots Cl^-$ ion pairs formed in $K(np)/CCl_4$ collisions for the quantum numbers n and Rydberg atom velocities indicated.

partly because the exponential translational energy release distribution peaks at $\epsilon = 0$. The most probable relative velocity of a $K^+ \cdots Cl^-$ ion pair is therefore approximately equal to that of the parent $K^+ \cdots CCl_4^*$ ion pair at the time of dissociation. The resulting decrease in the reduced mass of the ion pair following dissociation leads to a decrease in the kinetic energy of relative motion. As a result, even $K^+ \cdots CCl_4^*$ ion pairs that are initially unbound can form bound $K^+ \cdots Cl^-$ ion pairs after dissociation. At low Rydberg atom velocity, the peaks in the distribution of $K^+ \cdots Cl^-$ binding energy are near the binding energy of the parent Rydberg states, because elec-

tron capture occurs near the outer classical turning point where the radial electron probability density is maximal.

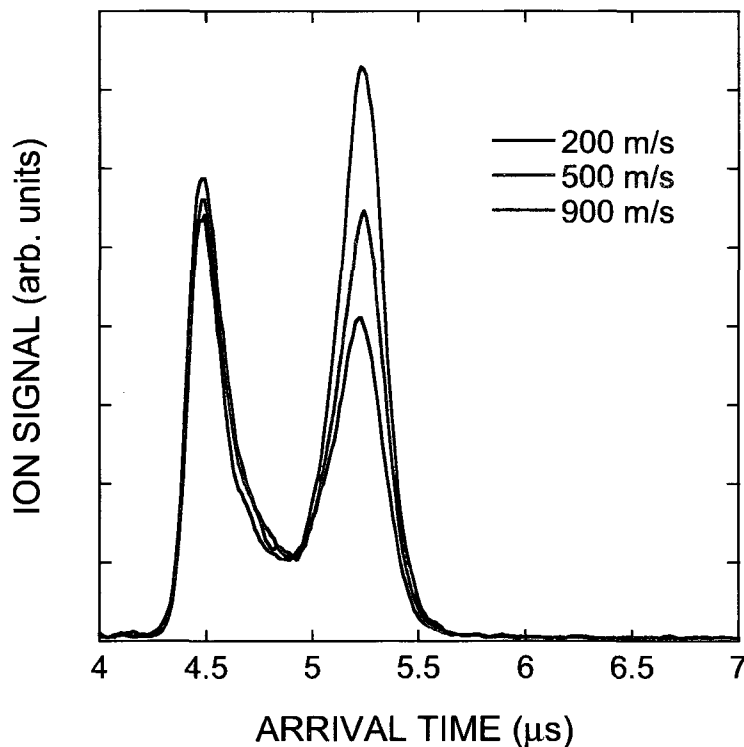


Figure 4.2 : Time-of-flight spectra of Cl^- ions observed in $\text{K}(20p)/\text{CCl}_4$ collisions for the Rydberg atom velocities indicated. The first peaks are associated with field-detached Cl^- ions from bound ion pairs and free ions created during the ramp, while the second peaks result from the arrival of initially unbound Cl^- ions.

The time-of-flight spectrometer is used to discriminate the ions with different binding energies. The arrival time distributions of Cl^- ions produced in $\text{K}(20p)/\text{CCl}_4$ collisions for the Rydberg atom velocities indicated are shown in Fig. 4.2. The spectra show separate peaks associated with initially unbound ion pairs and bound ion pairs. The first peaks are associated with field-detached Cl^- ions from bound ion pairs and free ions created by the $\text{K}(20p)/\text{CCl}_4$ collisions during the ramp, while the second

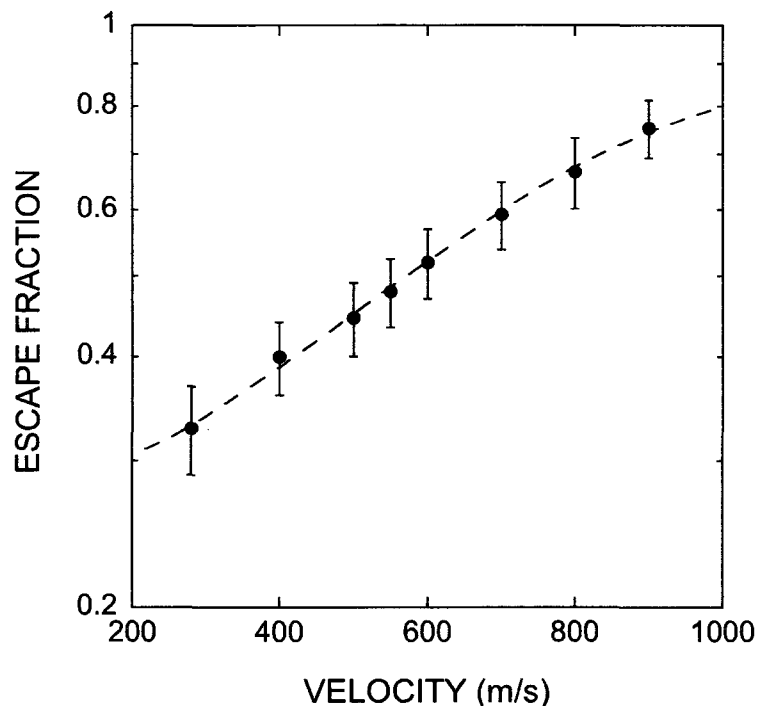


Figure 4.3 : The Rydberg atom velocity dependence of the escape fraction observed in $K(20p)/CCl_4$ collisions. The line shows the model prediction.

peaks result from the arrival of initially unbound Cl^- ions. Free ions are accelerated out of the interaction region at the beginning of the pulsed field. These ions gain little energy from the field. As the field is increased, bound ion pairs undergo field-induced detachment and the resulting free ions experience larger accelerations as they are extracted. They thus gain more energy from the field and arrive at the detector earlier than ions that were initially unbound. More unbound ion pairs are detected as the Rydberg atom velocity is increased, consistent with the productions in Fig. 4.1. The velocity dependence of both the calculated and observed escape fractions is shown in Fig. 4.3. The escape fractions are strongly dependent on Rydberg atom velocity and

vary from $\sim 30\%$ to $\sim 80\%$ as the Rydberg atom velocity increases from 200 m s^{-1} to 900 m s^{-1} . Good agreement is seen between the model predictions and experimental observations.

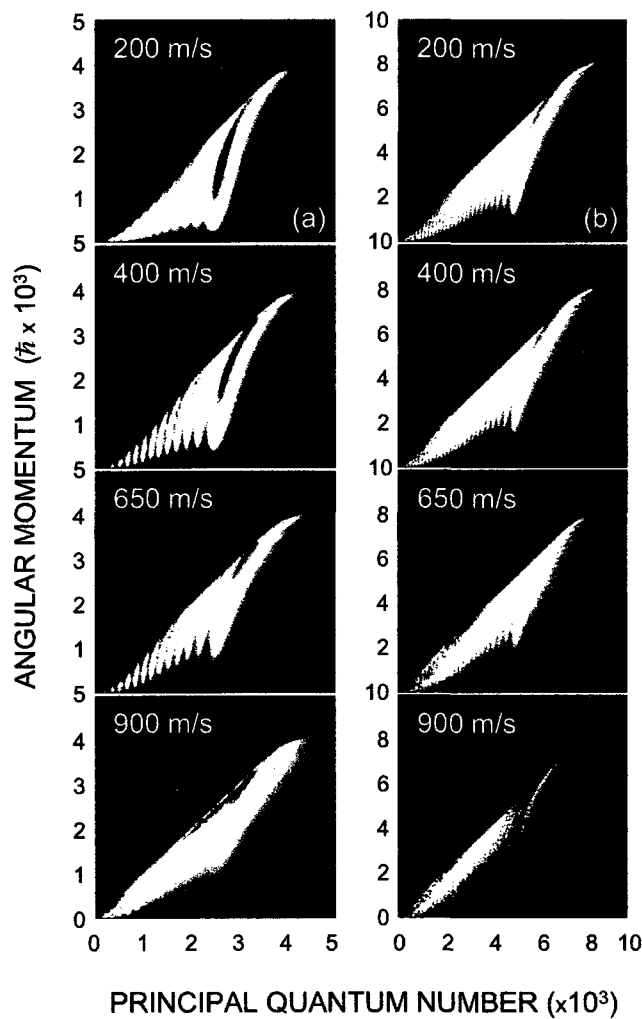


Figure 4.4 : Calculated distribution of n_H and ℓ_H of ion-pair states formed in (a) $\text{K}(16p)/\text{CCl}_4$ and (b) $\text{K}(30p)/\text{CCl}_4$ collisions for the Rydberg atom velocities indicated.

The results of model calculations showing the distribution of the principal quantum number n_H and angular momenta quantum number ℓ_H of bound heavy-Rydberg

ion pairs are presented in Fig. 4.4, for the Rydberg atom velocities indicated. The principal quantum number n_H of bound ion pairs is given by

$$n_H = (-R_H/E_B)^{1/2} \quad (4.2)$$

where E_B is the binding energy of the ion-pair states. In each case, population of high- ℓ_H states is favored, suggesting a sizable fraction of initial capture events occur at large impact parameters, because the radial electron probability density associated with the parent Rydberg states peaks near the outer classical turning point leading to well separated K^+ and Cl^- ion pairs. On the other hand, increases in Rydberg atom velocity can increase the relative velocity of $K^+ \cdots Cl^-$ ion pairs, thereby decreasing the number of bound ion pairs formed. This results in the narrowing of the ℓ_H distribution and its focusing near the upper limit $\ell_{Hmax} = n_H - 1$. Increases in n also lead to stronger localization near ℓ_{Hmax} , especially at higher Rydberg atom velocities. At low Rydberg atom velocities, the structure associated with the nodes of the radial electron probability density distribution becomes apparent.

Fig. 4.5 shows the K^+ signals observed following $K(16p)/CCl_4$ collisions as a function of the pulsed electric field applied across the interaction region $\sim 3 \mu s$ after excitation, together with model calculations that take into account direct formation of unbound ion pairs, the field-induced dissociation of bound ion pairs, and field ionization of parent Rydberg atoms. Even at a very small applied field, a sizable K^+ signal is observed, associated with direct production of unbound ion pairs, which increases dramatically with the relative collision velocity. The K^+ signal rises steadily

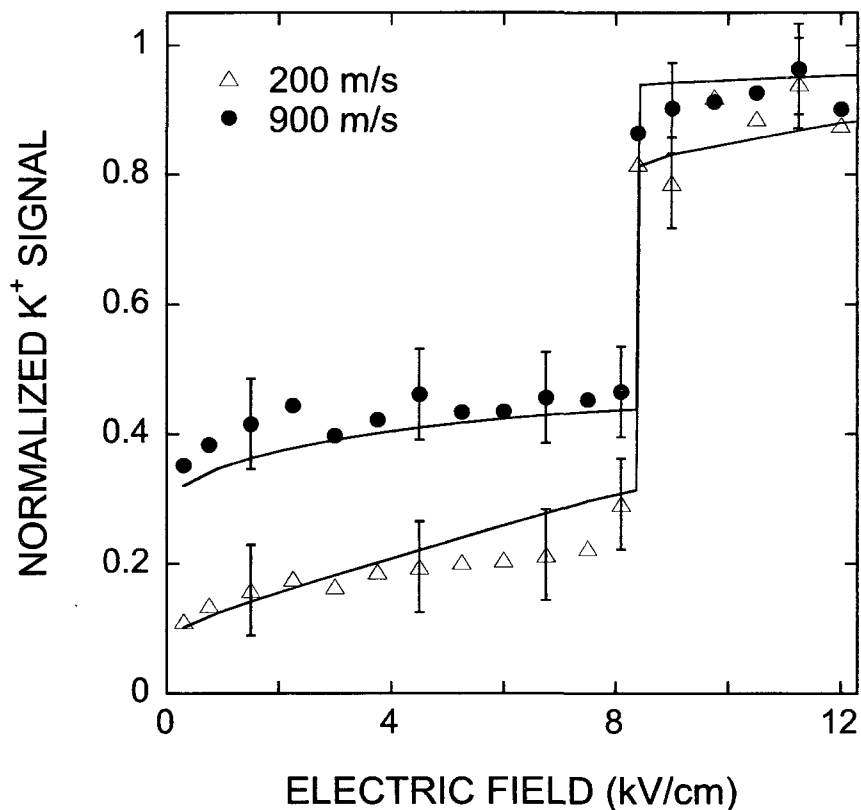


Figure 4.5 : K^+ signals observed following $K(16p)/CCl_4$ collisions as a function of applied field across the interaction region for the Rydberg atom velocities indicated. The solid lines show the model prediction.

with increasing fields, as a result of field-induced dissociation (The electric field can dissociate bound ion pairs). The fractional increase in the K^+ signal is greater at the lower Rydberg velocity (200 m s^{-1}) because a greater fraction of the product ion pairs is bound. The step-like increase in the ion signal occurs at a field of $\sim 8.4 \text{ kV cm}^{-1}$, and results from field ionization of the surviving parent Rydberg atoms. However, further small increases in the K^+ signal are observed at even higher fields, associated with dissociation of more strongly bound ion pairs.

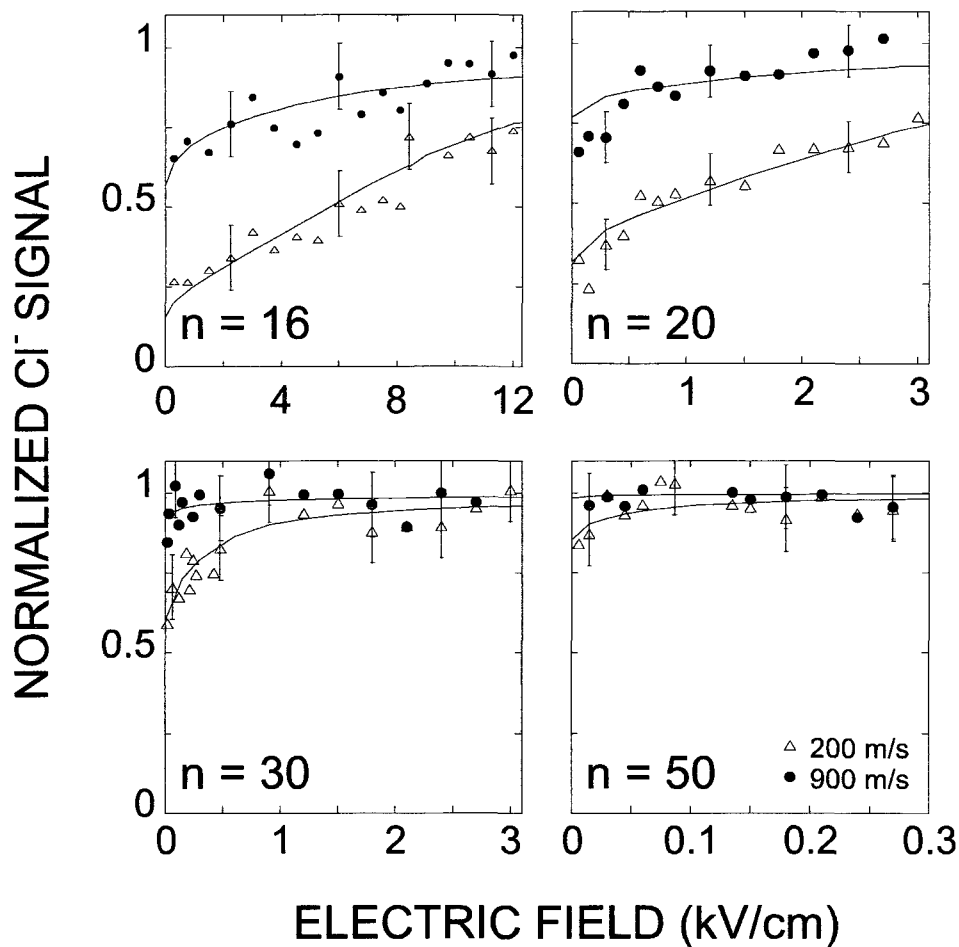


Figure 4.6 : Cl⁻ signals observed following K(np)/CCl₄ collisions for the quantum numbers n and Rydberg atom velocities indicated as a function of applied field. The solid lines show the model predictions.

The Cl⁻ signals observed following K(np)/CCl₄ collisions at $n = 16, 20, 30, 50$ as a function of applied electric field together with model predictions are shown in Fig. 4.6. At $n = 16$, similar behavior to that seen in Fig. 4.5 is observed in the Cl⁻ signal. A sizable signal is evident at low applied fields and results from direct formation of unbound ion pairs. The signal increases steadily with applied field due to field-induced dissociation. Continuing growth is seen even at the highest applied

fields, indicating they are not sufficient to dissociate all the bound ion pairs. This is particularly evident at the lower Rydberg atom velocity where the ion pairs are more strongly bound.

At $n = 50$, however, only at the lower Rydberg atom velocity is the creation of bound ion pairs seen. Even for a velocity of 200 m s^{-1} fewer than $\sim 15\%$ of the product ion pairs are bound, as shown in Fig. 4.1. Since these dissociate in small applied fields they must have weak binding energies. At $n = 30$ and low Rydberg atom velocities the bound fraction increases to $\sim 40\%$. Their binding energies are increased as demonstrated by the increasing fields required to induce dissociation. However, fewer than 10% of the ion pairs formed for a Rydberg atom velocity of 900 m s^{-1} are bound. At $n = 20$ noticeable numbers of bound ion-pair states are observed. The bound fraction is increased from $\sim 20\%$ to $\sim 70\%$ as the Rydberg atom velocity is decreased from 900 to 200 m s^{-1} . Increases in binding energy are also evident. Both the bound fraction and binding energies show further increases at $n = 16$. The good agreement between the experimental data and the model predictions justifies the assumptions, and the production of bound heavy-Rydberg ion-pair states is clearly demonstrated.

4.2 Lifetime Measurements

The lifetimes of ion-pair states formed in $\text{K}(np)/\text{CCl}_4$ collisions are investigated by field-induced dissociation. The effective lifetime of the parent Rydberg atoms in the

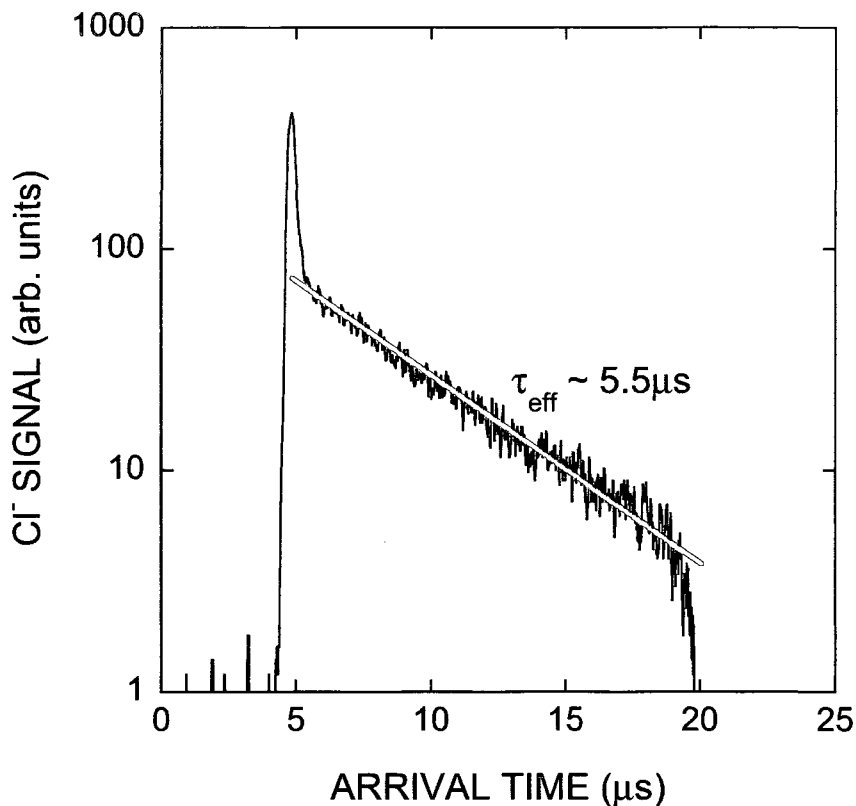


Figure 4.7 : Time-of-flight spectra of Cl^- signals observed following $\text{K}(16p)/\text{CCl}_4$ collisions with a small extraction field.

presence of target gas is first measured by monitoring the decay of the Cl^- signal resulting from direct formation of unbound ion pairs. Fig. 4.7 shows time-of-flight spectra for the Cl^- signal following $\text{K}(16p)/\text{CCl}_4$ collisions. Excitation to the $n = 16$ state occurs in zero field. $\sim 1 \mu\text{s}$ after the laser pulse, collision-produced free ions are collected by applying to the lower grid a $\sim 20 \mu\text{s}$ -wide extraction pulse that generates a field of $\sim 1.5 \text{ kV/cm}$ while the upper grid is kept grounded. This field is small compared to that required to field ionize parent Rydberg atoms ($\sim 8.3 \text{ kV/cm}$ at $n = 16$). The spectra show a sharp peak associated with the collection of those Cl^- ions

initially present. Following this onset the ion signal decays slowly as a consequence of the decay of the Rydberg atom population in the interaction region. An exponential fit to the data provides an effective lifetime τ of $\sim 5.5 \mu\text{s}$ for the parent Rydberg atoms.

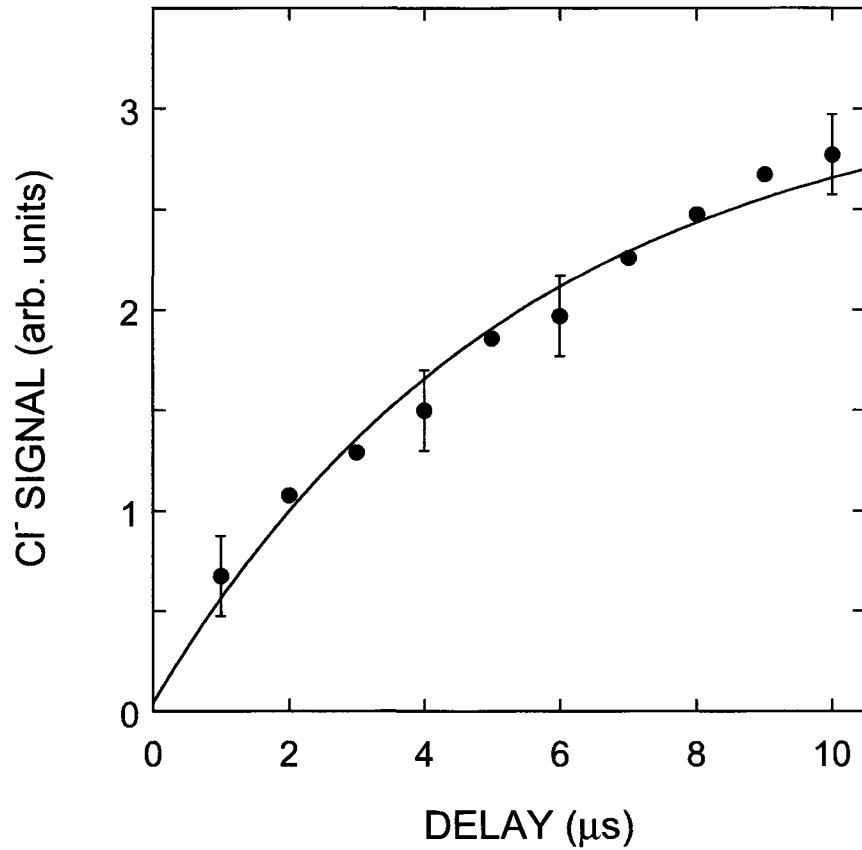


Figure 4.8 : Time development of the population of bound $\text{K}^+ \cdots \text{Cl}^-$ heavy-Rydberg ion-pair states.

The lifetime of the $\text{K}^+ \cdots \text{Cl}^-$ heavy-Rydberg ion-pair states is measured by observing the time development of their population through measurements of the Cl^- signals produced by field-induced dissociation. A small pulsed field ($\sim 0.15 \text{ kV/cm}$),

insufficient to induce detachment, is used to remove the Cl^- signal associated with direct formation of unbound ion pairs. The resulting signal is subtracted from that observed using a large pulsed field ($\sim 9.1\text{kV/cm}$). The arrival time distribution of bound ion-pair states produced in $\text{K}(16\text{p})/\text{CCl}_4$ collisions for a Rydberg atom velocity of 200 m s^{-1} is shown in Fig. 4.8 and steadily increases with the pulse delay. Assuming $\text{K}^+ \cdots \text{Cl}^-$ ion-pair states are infinitely long-lived, the time development of their population, $N(t)$, should be described by an equation of the form

$$N(t) = N_\infty(1 - e^{-t/\tau_{\text{eff}}}) \quad (4.3)$$

where τ_{eff} ($\sim 5.5\ \mu\text{s}$) is the effective lifetime of the parent Rydberg atoms in the presence of the target gas. The data can be well fit using a function of this form indicating the product ion-pair states are long-lived.

To further test the lifetime of the $\text{K}^+ \cdots \text{Cl}^-$ heavy-Rydberg ion-pair states, a series of differential measurements are undertaken by applying a second electric field, with the timing diagram shown in Fig. 3.3. Fig. 4.9 shows the time-of-flight spectra of Cl^- ion signals in $\text{K}(20\text{p})/\text{CCl}_4$ collisions for the Rydberg atom velocity of 200 m s^{-1} with the delays indicated before application of the second pulsed field. Collisions are allowed to occur for $\sim 1\ \mu\text{s}$ following Rydberg atom excitation before application of a voltage pulse of 1100 V to the lower interaction region grid. This pulse generates a field of $\sim 3.3\text{ kV cm}^{-1}$ which is well above the adiabatic field ionization threshold for $\text{K}(20\text{p})$ Rydberg atoms, $\sim 2.9\text{kV cm}^{-1}$. In addition to ionizing the parent Rydberg atoms, this field immediately extracts free Cl^- ions present in the interaction region

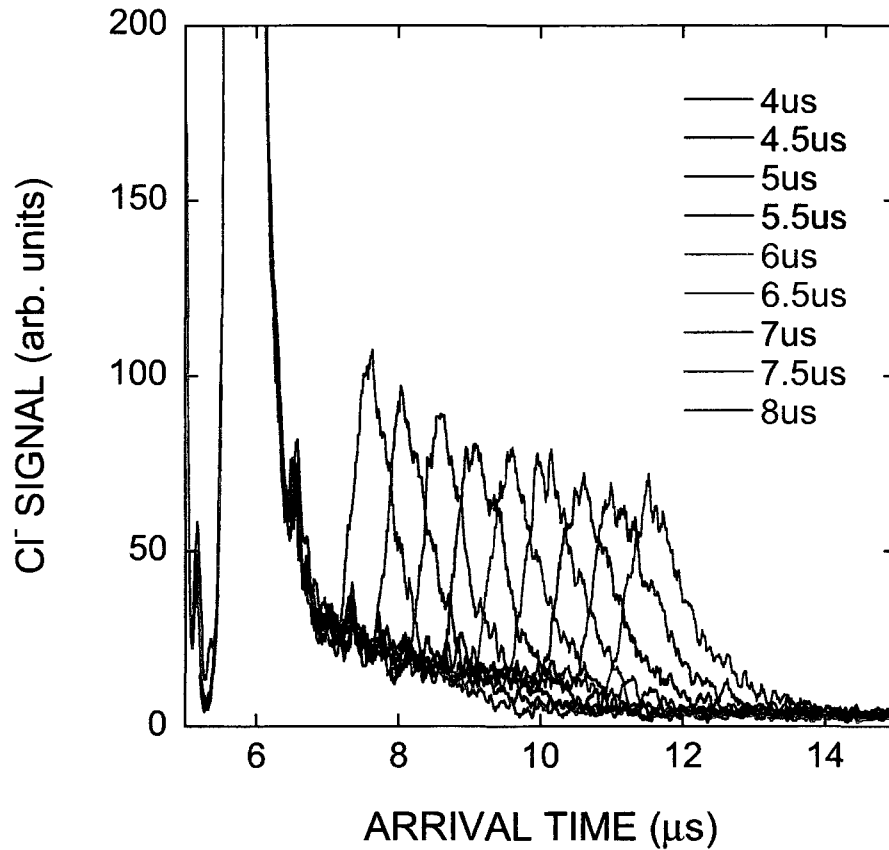


Figure 4.9 : Time-of-flight spectra of Cl^- ion signals produced in $\text{K}(20p)/\text{CCl}_4$ collisions at the Rydberg atom velocity of 200 m s^{-1} with the delay variation of the second pulsed fields indicated.

that results from direction production of unbound $\text{K}^+ \cdots \text{Cl}^-$ ion-pair states. It also dissociates $\text{K}^+ \cdots \text{Cl}^-$ bound ion-pair states with binding energies E_B up to $\sim 29 \text{ meV}$ generating additional Cl^- ions. The average binding energy E_B of ion-pair states dissociated diabatically by an electric field F is given in atomic units by

$$F = 1.5 \left(\frac{2E_B}{3} \right)^2 \quad (4.4)$$

although ion-pair states dissociated in any particular field F will have a range of

binding energies centered near this value E_B . Cl^- ions from both sources are detected by the PSD giving rise to the large peaks seen at around $\sim 6 \mu\text{s}$. Following a further (variable) time delay, another pulsed field $\sim 500 \text{ V}$ is applied to the upper interaction region grid giving a total net field of $\sim 4.8 \text{ kV cm}^{-1}$, sufficient to dissociate ion-pair states with binding energies E_B up to $\sim 34 \text{ meV}$. Application of the second pulsed field, therefore, results in dissociation of ion-pair states with binding energies E_B in the range of $\sim 29\text{-}34 \text{ meV}$. This results in a second peak in the arrival time distribution, demonstrating the presence of $\text{K}^+ \cdots \text{Cl}^-$ ion-pair states with binding energies in this range.

A small Cl^- signal decaying exponentially after application of the first pulsed field is observed. If all the parent Rydberg atoms initially present in the interaction region would be destroyed by the first pulsed field, no further Cl^- production would occur. However, tests without the target gas present indicate that not all the Rydberg states initially present are ionized by the first pulsed field. First, a small fraction of the parent Rydberg atoms do not follow exactly adiabatic paths to ionization and can only be ionized at higher fields. Second, a small number of the parent Rydberg atoms radiatively decay to more tightly bound lower n states before application of the first pulsed field. Therefore, collisions between the remaining Rydberg atoms and the target molecules give rise to the small Cl^- signal following the main peaks.

The size of the Cl^- signal resulting from application of the second pulsed fields in Fig. 4.9 changes little with its time delay. Further studies shown in Fig. 4.10 provide

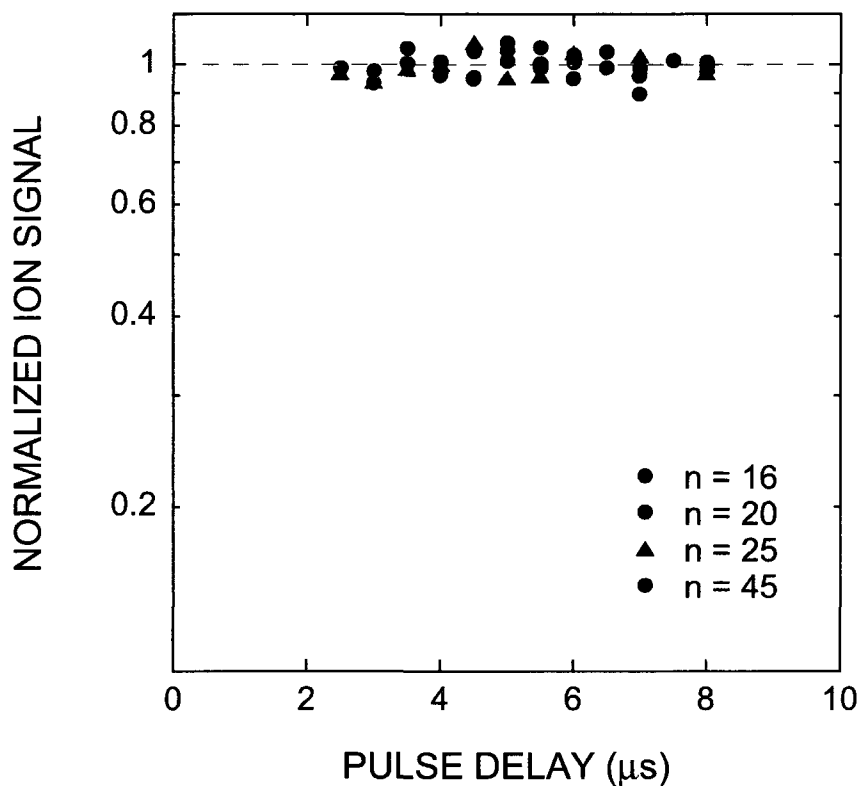


Figure 4.10 : Time development of the population of bound $K^+ \cdots Cl^-$ heavy-Rydberg ion-pair states dissociated by the second pulsed field for the value of n indicated.

the time development of the population of tightly bound $K^+ \cdots Cl^-$ heavy-Rydberg ion-pair states dissociated by the second pulsed fields at the Rydberg atom velocity of 200 m s^{-1} for Rydberg atom principal quantum numbers $n = 16, 20, 25, 45$. The corresponding binding energies E_B for each n have the ranges 44-48, 29-34, 18-23, 5-12 meV. In each case no significant decay of the Cl^- signal is observed, an indication that $K^+ \cdots Cl^-$ heavy-Rydberg ion pairs formed in $K(np)/CCl_4$ collisions are long-lived. This long lifetime can be explained partly from the angular momentum distribution. In contrast to photoexcitation where selection rules only allow formation

of a limited number of low-angular-momentum states, Rydberg atom collisions preferentially populate high-angular-momentum states. The K^+ and Cl^- ions therefore remain relatively far apart, reducing the possible overlap between their wavefunctions and the likelihood of charge transfer and neutralization. No internal vibrational or rotational energy is released in the Cl^- ion to induce dissociation of the ion pairs, which also leads to a long lifetime.

4.3 Orbital Properties

To better understand the long lifetime of bound $K^+ \cdots Cl^-$ ion pairs, the orbital properties of bound heavy-Rydberg ion-pair states following $K(np)/CCl_4$ collisions are investigated by a Monte Carlo collision code described in section 2.5. Fig. 4.11 shows the calculated distribution of heavy-Rydberg principal quantum number n_H and angular momentum quantum number ℓ_H of bound $K^+ \cdots Cl^-$ ion-pair states formed in $K(np)/CCl_4$ collisions for the Rydberg atom velocity of 200 m s^{-1} and the values of n indicated. This distribution expands as the Rydberg atom quantum number n increases, resulting from the expanding size of the electron cloud for the Rydberg atoms. Increases in quantum number n also lead to the narrowing of the ℓ_H distribution and its focusing near the upper limit $\ell_{H\max} = n_H - 1$. Therefore electron transfer favors formation of high- ℓ_H ion-pair states as n increases.

Calculated angular momentum distributions for bound heavy-Rydberg ion-pair states formed in $K(16p)/CCl_4$ collisions for the Rydberg atom velocities indicated

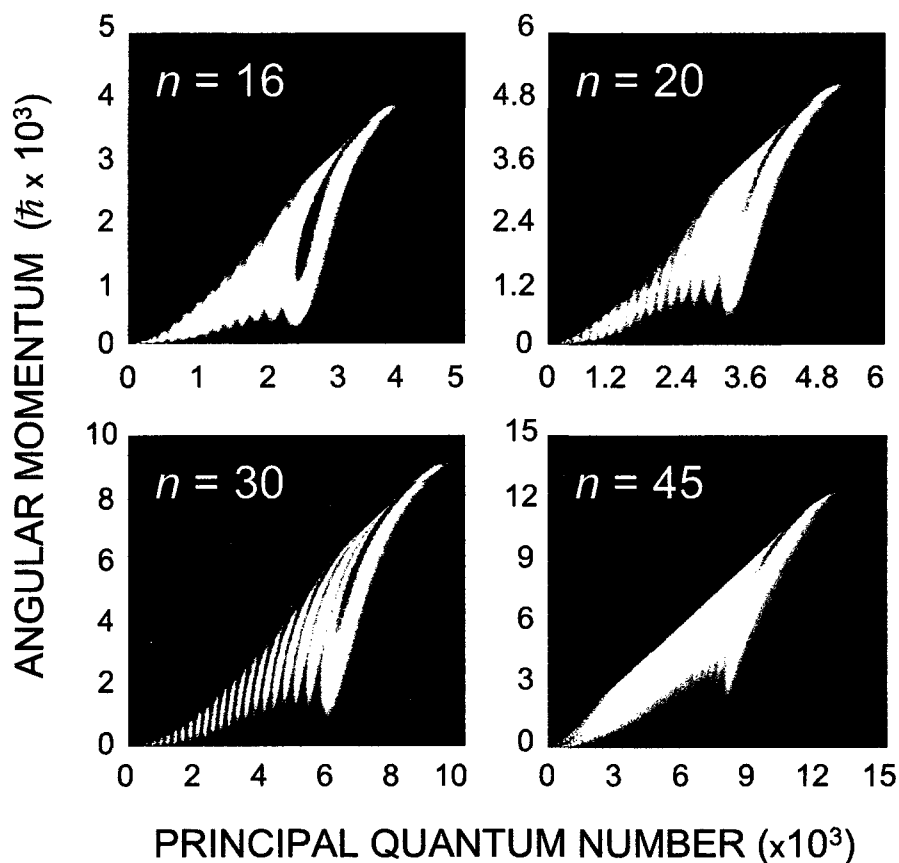


Figure 4.11 : Calculated distribution of n_H and ℓ_H of ion-pair states formed in $K(np)/CCl_4$ collisions for a Rydberg atom velocity of 200 m s^{-1} and the values of n indicated.

are shown in Fig. 4.12. The product ion pairs have a broad distribution of angular momenta, which significantly depends on the Rydberg atom velocity. This results from the large distribution of impact parameters and the fact that electron capture occurs over a range of distance from the K^+ core ion.

Calculated periapsis distributions for heavy-Rydberg ion-pair states formed in $K(16p)/CCl_4$ collisions for the Rydberg atom velocities indicated are shown in Fig. 4.13. The distribution of the closest separation of the ion pairs at periapsis covers a broad

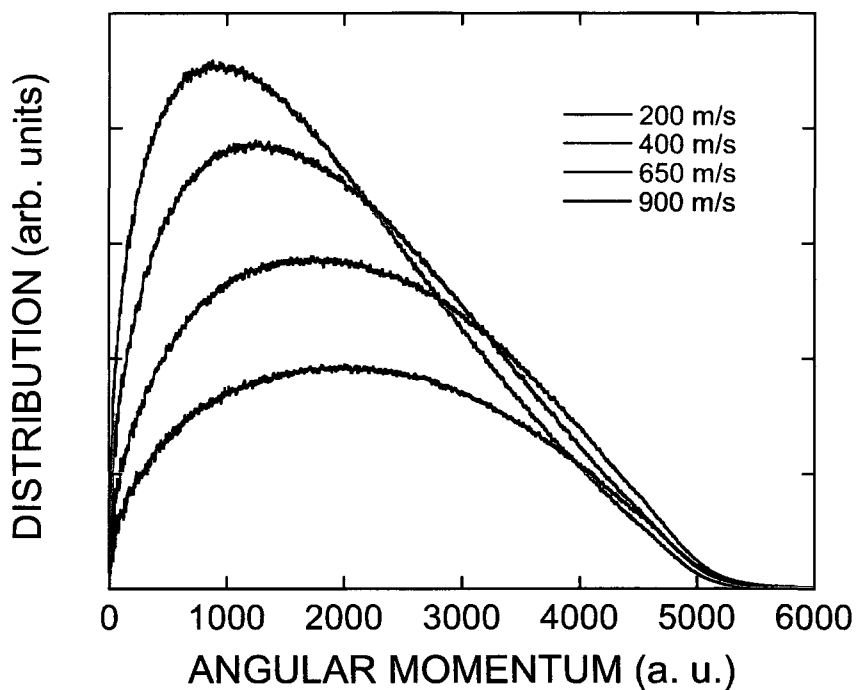


Figure 4.12 : Calculated angular momentum distribution of heavy-Rydberg ion-pair states formed in $K(16p)/CCl_4$ collisions for the Rydberg atom velocities indicated.

range, but peaks near zero. This separation does not scale linearly with the angular momentum, and all the states with lower angular momentum have relatively small separations at periapsis. Though many product ion pairs pass relatively close to each other they do not undergo internal-to-translational energy transfer as $K^+ \cdots SF_6^-$ ion pairs do. Furthermore, decay through the mutual neutralization of the K^+ and Cl^- ions in a close collision is highly non-resonant, leading to very small rates of charge transfer and separation as ground-state K and Cl atoms.

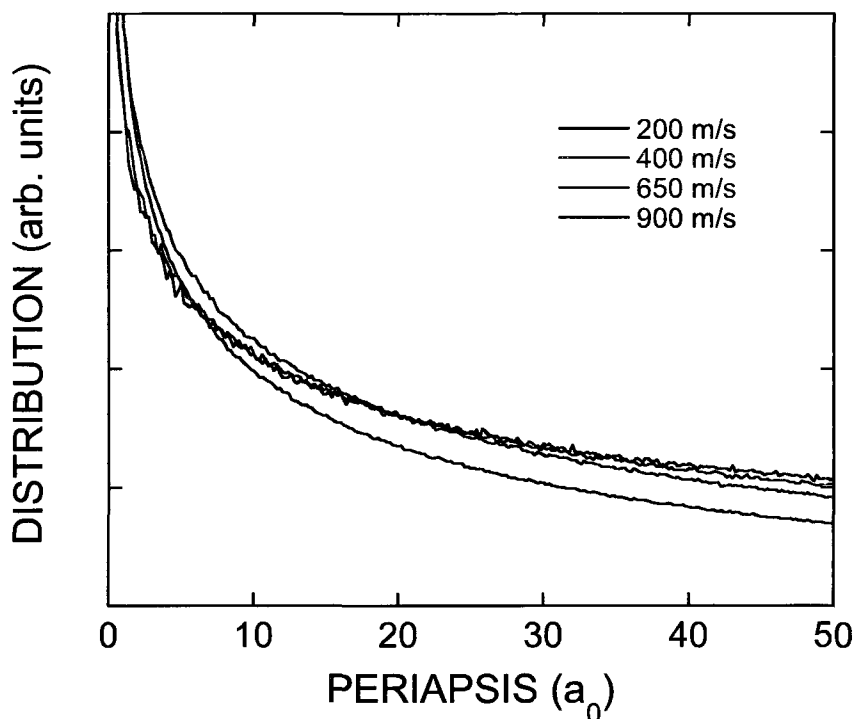


Figure 4.13 : Calculated periapsis distribution of heavy-Rydberg ion-pair states formed in $K(16p)/CCl_4$ collisions with the Rydberg atom velocities indicated.

4.3.1 Collinear Beams

The present experimental work demonstrates the formation of weakly-bound heavy-Rydberg ion-pair states through Rydberg atom collisions with background target gases. To further explore heavy-Rydberg states with low angular momentum whose physical properties may be different from those of states with high angular momentum, calculations are undertaken for collinear potassium and molecular beams. The target species adopted, SF_6 , non-dissociatively attaches low-energy electrons leading

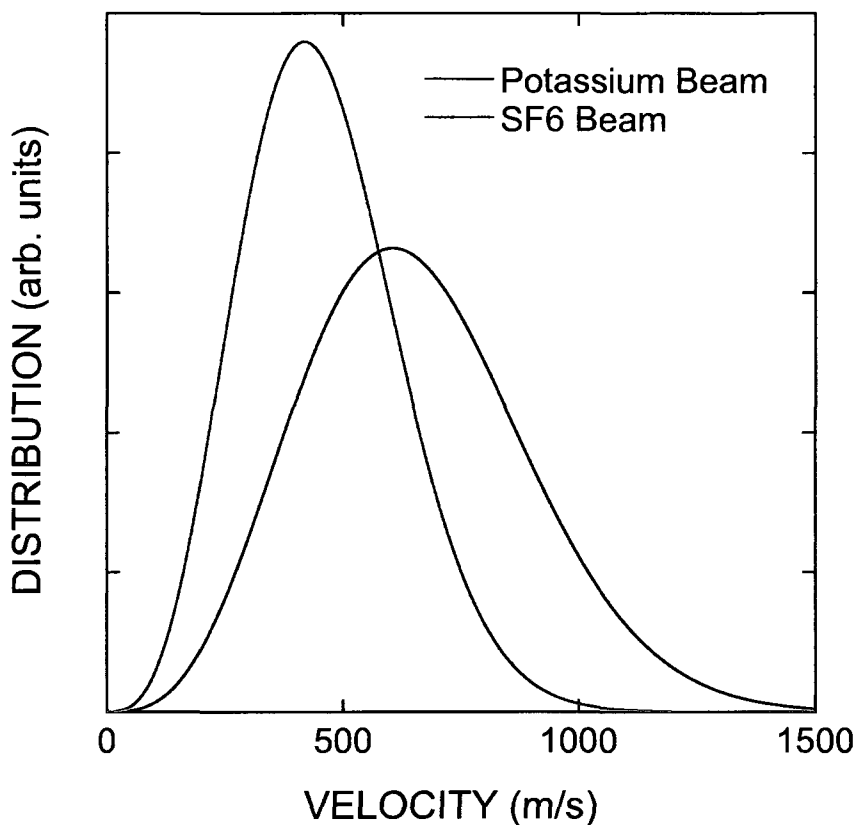
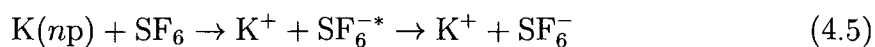


Figure 4.14 : Velocity distributions of potassium atomic and SF₆ molecular beams.

to the electron transfer reactions of the type:



where SF₆⁻ is a long-lived ($\tau \sim 1-10$ ms) but metastable anion. Fig. 4.14 shows the velocity distributions of potassium and SF₆ beams respectively, where potassium atoms are heated up to 300°C in the oven and the temperature of attaching SF₆ molecules is set at the room temperature. The large overlap in these distributions indicates if two beam are aligned collinearly, the relative velocity of collision pairs

can be significantly reduced, especially at the low Rydberg atom velocity. Fig. 4.15 shows the relative velocity distributions of bound $\text{K}^+ \cdots \text{SF}_6^-$ ion pairs formed in $\text{K}(16\text{p})/\text{SF}_6$ collisions for (a) the background target gas and (b) collinear interacting beams with Rydberg atom velocities indicated. For each Rydberg atom velocity, the relative velocity distribution of bound heavy-Rydberg ion pairs produced for collinear beams is substantially lower than that for a background target gas, a direct result of the reduced relative velocity of collision pairs. At a Rydberg atom velocity of 200 m s^{-1} , this relative velocity distribution peaks near zero, which indicates that most bound ion pairs have only small relative velocities in their center-of-mass frame. The reduced relative velocity also decreases the kinetic energy of the bound ion pairs, making other interactions of bound ion-pair states observable. This method opens up new approaches to exploring heavy-Rydberg ion-pair states following Rydberg atom collisions with attaching targets.

Fig. 4.16 illustrates the angular momentum distributions of $\text{K}^+ \cdots \text{SF}_6^-$ bound heavy-Rydberg ion-pair states formed in $\text{K}(16\text{p})/\text{SF}_6$ collisions using (a) a background target gas and (b) collinear interacting beams. The angular momentum distribution of bound heavy-Rydberg ion pairs peaks near zero for the low Rydberg atom velocities, attributed to the same features for the relative velocity distribution of bound ion pairs.

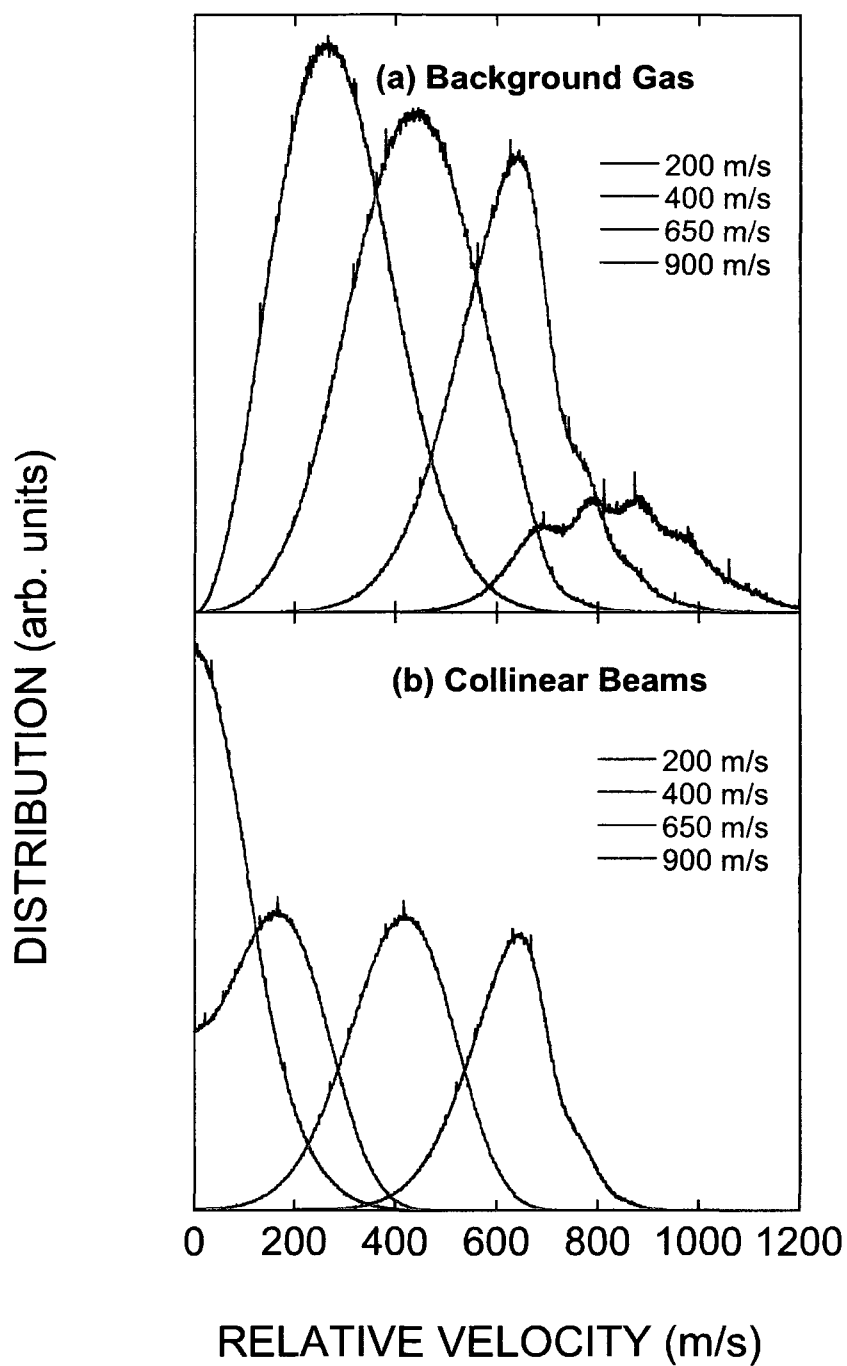


Figure 4.15 : Relative velocity distributions of bound ion pairs formed in $K(16p)/SF_6$ collisions for (a) a background target gas and (b) collinear interacting beams and the Rydberg atom velocities indicated.

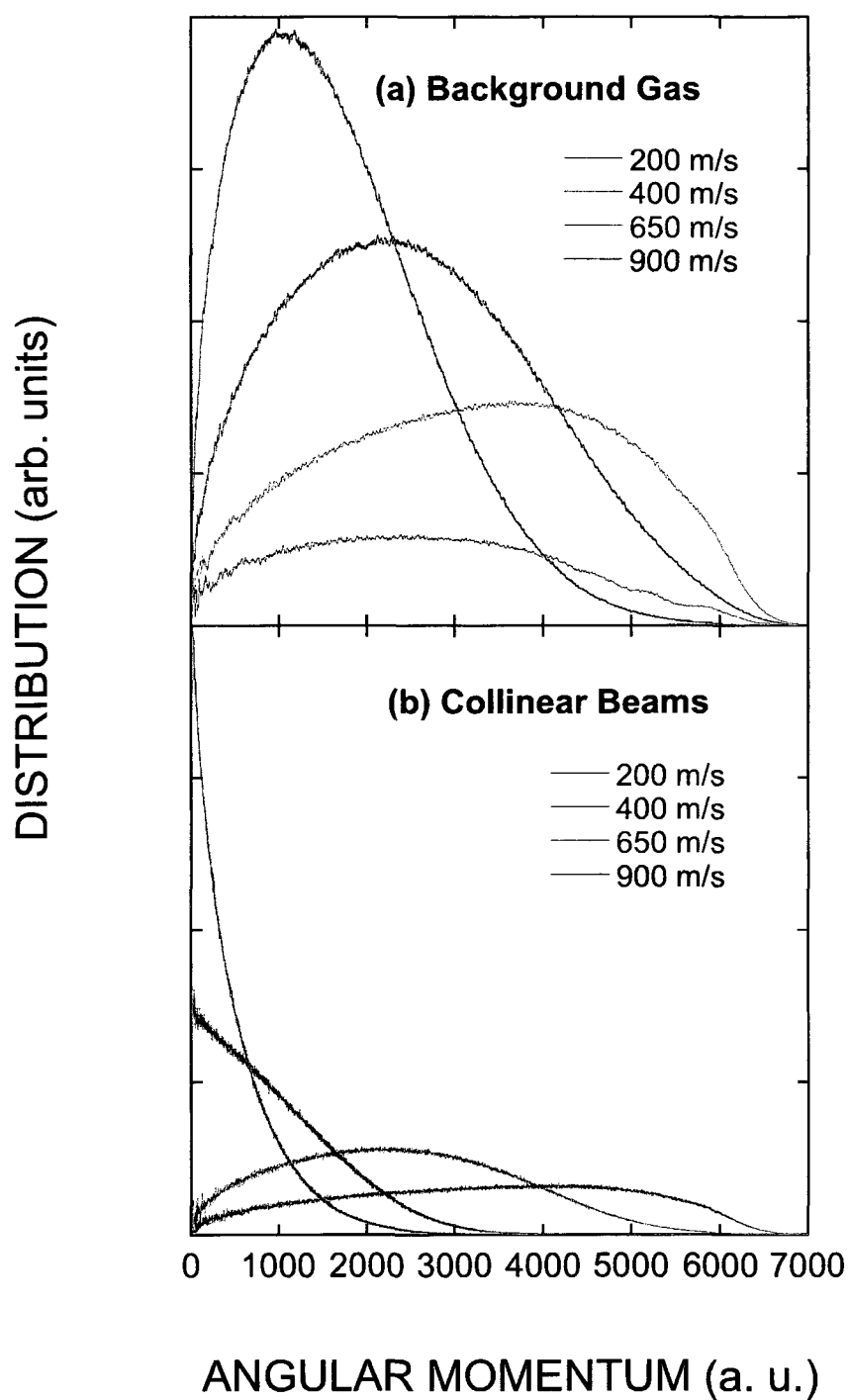


Figure 4.16 : Angular momentum distributions of bound ion pairs formed in $K(16p)/SF_6$ collisions using (a) a background target gas and (b) collinear beams and the Rydberg atom velocities indicated.

Chapter 5

Conclusions and Future Work

5.1 Conclusions

The present experiments and calculations demonstrates formation of bound heavy-Rydberg ion-pair states through Rydberg atom collisions with attaching target gases. The calculated broad distribution of binding energies of $\text{K}^+ \cdots \text{Cl}^-$ ion pairs indicates both bound and free products are formed through collisions. The bound ion pairs also have a broad distribution of heavy-Rydberg quantum number n_{H} and angular momentum quantum number ℓ_{H} , which is dependent on the Rydberg atom velocity and its quantum number n . Electric field-induced dissociation is used to explore the energy distribution and the lifetime of the ion pairs. Long-lived $\text{K}^+ \cdots \text{Cl}^-$ ion pairs are observed and no evidence of their decay is seen. Calculations on the angular momentum of ion-pair states formed in collinear collisions with potassium and SF_6 beams shows the formation of ion-pair states with low angular momentum.

5.2 Future Work

These experimental and computational methods can be extended to other molecular species which attach low energy electrons. Interesting targets include SF_6 , C_6F_6 , c-

C_7F_{14} and BrCN. Some molecules, such as SF_6 , exhibit vibrational-to-translational energy transfer which can dissociate bound ion-pair states. Some molecules, such as BrCN, which is in the ground vibrational state, also have rotational modes with energies sufficient to dissociate bound ion-pair states.

Future experiments can also explore heavy Rydberg states with extreme low angular momentum quantum numbers by using collinear potassium and molecular beams. Because relative velocity is significantly reduced, it can lead to detailed studies of electron attachment.

Bibliography

- [1] E. Reinhold and W. Ubachs *Molec. Phys.*, vol. 103, p. 1329, 2005.
- [2] R. C. Shiell, E. Reinhold, F. Magnus, and W. Ubachs *Phys. Rev. Lett.*, vol. 95, p. 213002, 2005.
- [3] M. Cannon, C. H. Wang, and F. B. Dunning *Chem. Phys. Lett.*, vol. 479, p. 30, 2009.
- [4] T. F. Gallagher, *Rydberg Atoms*. Cambridge: Cambridge University Press, 1994.
- [5] P. M. Koch, *Rydberg States of Atoms and Molecules*. New York: Cambridge University Press, 1983.
- [6] J. A. Schiavone, S. M. Tarr, and R. S. Freund *Phys. Rev. A*, vol. 20, p. 71, 1979.
- [7] C. J. Foot, *Atomic Physics*. New York: Oxford University Press, 2005.
- [8] L. G. Christophorou, D. L. McCorkle, and A. A. Christodoulides, "Electron attachment processes," in *Electron-Molecule Interactions and Their Applications*, vol. 1, ch. 6, New York: Academic Press, 1984.
- [9] R. A. Popple, C. D. Finch, K. A. Smith, and F. B. Dunning *J. Chem. Phys.*, vol. 104, p. 8485, 1996.

- [10] C. D. Finch, R. Parthasarathy, H. C. Akpati, P. Nordlander, and F. B. Dunning *J. Chem. Phys.*, vol. 106, p. 9594, 1997.
- [11] R. A. Popple, C. D. Finch, and F. B. Dunning *Int. J. Mass Spectrom. Ion Processes*, vol. 149/150, p. 37, 1995.
- [12] X. Ling, M. A. Durham, A. Kalamarides, R. W. Marawar, B. G. Lindsay, K. A. Smith, and F. B. Dunning *J. Chem. Phys.*, vol. 93, p. 8669, 1990.
- [13] C. W. Walter, K. A. Smith, and F. B. Dunning *J. Chem. Phys.*, vol. 90, p. 1652, 1989.
- [14] K. A. Smith, "Position-sensitive particle detection with microchannel-plate electron multipliers," in *Atomic, Molecular, and Optical Physics: Charged Particles*, San Diego: Academic Press, 1997.
- [15] N. F. Ramsey, *Molecular Beams*. Oxford: Oxford University Press, 1956.

Appendix A

Calculations of the Potassium Beam Density

In the main chamber, a hot wire is used to check the potassium beam density. The hot wire is a tungsten wire 0.005 inch in diameter, 5 cm long, heated by a current of ~ 0.7 A. Its operating temperature is approximately 1500 K, roughly estimated by equating electric power dissipation through the wire and the radiation loss

$$I^2 R = \epsilon \sigma A T^4 \quad (\text{A.1})$$

where ϵ is the Stefan-Boltzmann constant ($5.67 \times 10^{-8} \text{ W} \cdot \text{m}^{-2} \cdot \text{K}^{-4}$), σ is the emissivity of tungsten (~ 0.2 at 1500 K) and A is the surface area of the tungsten wire.

The sketch of the hot wire detector is shown in Fig. A.1. Given the tungsten work function is 4.64 eV whereas the ionization energy of a potassium atom is 4.34 eV, it is easier to strip an electron from a potassium atom than to pull an electron out of a clean tungsten surface. Therefore, when a potassium atom approaches the heated tungsten wire, it tends to lose its valence electron and become ionized. The ion is then held onto the conducting surface until it picks up enough thermal energy from the hot wire to escape as a free ion. The probability that an atom escapes from a

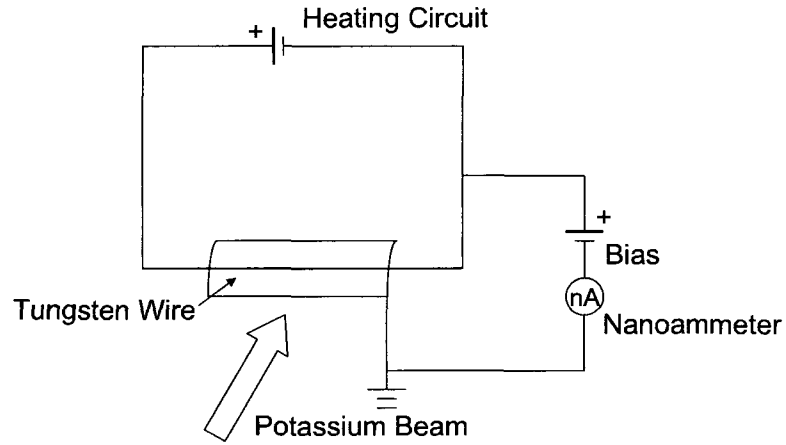


Figure A.1 : Sketch of the hot wire detector.

clean surface as an ion is given by the Saha-Langmuir equation

$$P = \frac{1}{1 + 2 \exp\left(\frac{\Lambda - \Phi}{k_B T}\right)} \quad (\text{A.2})$$

where Λ is the ionization energy of an incident atom, Φ is the work function of the surface and T is the temperature of the surface. For a clean tungsten surface at $T \sim 1500$ K, 83.5% of the incident potassium atoms will escape as ions. A positive bias on the hot wire prevents the ions from falling back. The saturated ion current is proportional to the rate of potassium atoms striking the hot wire, giving the potassium beam density at the wire as

$$n_b = \frac{i}{b\phi\bar{v}qP} \quad (\text{A.3})$$

where i is the ion current, b is the width of the potassium beam at the wire, ϕ is the wire diameter, \bar{v} is the average velocity of the potassium beam, q is the charge

a potassium ion carries, and P is the ionization probability. In the experiment, i is $\sim 3 \times 10^{-9}$ A, b is ~ 2.95 mm near the wire, $\phi = 0.005$ inch, $\bar{v} = 557$ m/s, $q = 1.6 \times 10^{-19}$ C, and $P = 0.835$, giving $\sim 0.11 \times 10^9$ cm $^{-3}$ for the potassium beam density near the hot wire (which corresponds to 0.8×10^9 cm $^{-3}$ at the center of the interaction region).